A practical engineering method to map microclimate-driven degradation risks on building façades

(article starts on next page)

Building and Environment 302 (2026) 114848

Contents lists available at ScienceDirect

Building and Environment

journal homepage: www.elsevier.com/locate/buildenv

A practical engineering method to map microclimate-driven degradation risks on building façades

Jan Mandinec *, Angela Sasic Kalagasidis, Pär Johansson

Department of Architecture and Civil Engineering, Chalmers University of Technology, SE-412 96 Gothenburg, Sweden

ARTICLE INFO

Keywords:
Hygrothermal simulation
Freeze-thaw degradation
Façade microclimate
Moisture induced degradation
Risk assessment
Wind-driven rain (WDR)

ABSTRACT

Assessing moisture-induced degradation risks across façades typically relies on Computational Fluid Dynamics (CFD) to resolve wind-driven rain (WDR) distribution and spatially varying microclimate conditions. This paper presents an alternative engineering-based methodology combining semi-empirical WDR models with detailed solar irradiation analysis to derive spatially varying boundary conditions for hygrothermal simulations. Freeze-thaw performance indicators are then used to estimate degradation risks, enabling spatial mapping of façade vulnerability.

The methodology is demonstrated on a brick façade in Gothenburg, Sweden, where degradation had been previously documented across 104 façade sections. Two WDR models—ISO 15927-3:2009 and Straube-Burnett (SB)—were applied over a 31-year simulation period. The ISO model at a 75% relative humidity (RH) threshold—used as the criterion for counting freeze-thaw cycles—showed the strongest agreement with observed degradation patterns (PCC = 0.6). The SB model required a higher RH threshold (90%) to achieve moderate agreement (PCC = 0.32). These differences highlight how RH thresholds act as compensating parameters for differences in modeled moisture load rather than direct indicators of critical saturation. Similar correlation levels were obtained with a second brick type, using 85% RH thresholds for both models, indicating that façade microclimate, rather than material properties, dominates the spatial distribution of degradation.

The results show that the proposed methodology can reproduce key spatial patterns of degradation risk without CFD, although the absolute risk quantification remains limited. The methodology offers designers, consultants, and building owners a cost-efficient basis for prioritizing inspections, maintenance planning, and retrofit strategies by identifying the most microclimate-vulnerable façade sections.

1. Introduction

Today, many renovation decisions are taken only after degradation occurs. In Sweden, for example, approximately 70% of renovation actions are initiated after a component has exceeded its service life [1]. Although this reactive approach is straightforward, it is economically suboptimal compared with proactive renovation strategies. Farahani et al. [2] estimate that, in the Swedish context, optimizing the timing of interventions relative to component condition states can reduce renovation costs by up to 15%.

Proactive renovation planning requires deterioration models that describe how a component's condition evolves over time. A common modelling approach is to use the power-law function [3], where deterioration is expressed as a time-dependent function with empirically derived parameters that implicitly account for material properties, environmental exposure, and usage conditions. For building façades, however, renovation planning is often based on visual inspections, using predefined rating scales [4–6] or performance metrics such as severity of degradation [7] or overall degradation level [8]. These observations can be used to estimate future deterioration through Markov chain models for rating scales [9,10], or fuzzy and multiple regression approached for performance-based indicators [11,12] supporting more efficient maintenance scheduling.

A common limitation to these approaches is that they overlook the actual moisture performance of the façade. Moisture exposure can increase heat losses [13,14] and accelerate material deterioration [15]. Consequently, façades—or sections of them—may require renovation earlier than expected, leading to unnecessary maintenance costs.

* Corresponding author.
E-mail address: jan.mandinec@chalmers.se (J. Mandinec).

https://doi.org/10.1016/j.buildenv.2026.114848
Received 20 March 2026; Received in revised form 11 May 2026; Accepted 29 May 2026
Available online 5 June 2026

1.1. Limitations and applicability of hygrothermal performance indicators

Technical standards are typically used to minimize the risk of moisture-induced deterioration. In Sweden, this is supported by ByggaF [16], a qualitative moisture-risk assessment framework that provides procedures and checklists for a building's production and operation stages. Complementing these qualitative methods are hygrothermal performance indicators, which quantify moisture risk directly from hygrothermal simulation outputs. Such indicators, formulated as dose-response functions, are primarily applied during the design stage to evaluate risks related to biological growth [17] and freeze-thaw (F-T) damage [18]. Despite their widespread use, localized F-T degradation is still frequently observed across façades.

A key limitation is that hygrothermal modeling alone cannot predict onset of degradation: it can only provide relative risk between design alternatives. However, F-T performance indicators (e.g., the number of moist F-T cycles) have been shown to correlate with damage progression in both bricks [19–21] and mortar [22,23]. They may therefore serve as practical proxies for more advanced but rarely used coupled hygrothermal-mechanical models [24], offering a simpler means of estimating both the onset and progression of deterioration.

Transferring laboratory-based correlations to real façades is challenging. Technical standards for frost-resistance tests (e.g., EN 12371:2010, EN 772-18:2011, SIS-CEN/TS 772-22:2008) prescribe uniform exposure conditions—fixed freezing/thawing durations and complete specimen saturation—that do not reflect the heterogeneous moisture conditions on actual façades. Mensinga [25,26] attributes discrepancies between laboratory predictions and in-situ performance to inadequate moisture control and omnidirectional frost exposure, which can cause some bricks to outperform expectations in real application. Consequently, the number of moist F-T cycles required for damage initiation on real façades remains uncertain. This uncertainty extends to other F-T indicators such as the modified winter index [27] and the F-T damage risk index [28].

Where and to what extent degradation occurs on a façade is governed by the interplay between local microclimate and material properties. For brick façades, microclimate—driven by façade orientation, exposure and surrounding obstructions—controls the spatial variation in wetting and drying, while material variability influences moisture absorption behavior, hygrothermal response, and critical moisture saturation. Ideally, both factors should be represented through models distributed across the façade, enabling observed localized degradation to be linked to hygrothermal performance indicators. This study examines how microclimate variations influence the occurrence and spatial distribution of façade degradation.

1.2. Modeling spatial variations of façades microclimate

In practice, hygrothermal assessments commonly assign one set of boundary conditions to the entire façade, accounting for microclimate only through façade orientation. However, several methods and tools exist to capture differences in solar irradiation, longwave sky-radiation cooling, and wind-driven rain (WDR) across façades.

Radiation-related microclimate effects are relatively straightforward to model using radiosity or ray-tracing algorithms combined with different diffuse sky models [29]. Tools such as Ladybug [30], De Luminae [31], and INDALUX [32] provide detailed radiation analyses while accounting for shading from surrounding obstructions.

Estimating WDR is considerably more challenging due to the complexity of multiphase flow between wind and raindrops. Semi-empirical models (most notably ISO 15927-3:2009 and ASHRAE 160P, based on the Straube-Burnett (SB) model [33]) are limited to a small number of façade configurations and only superficially consider surroundings. The SB model ignores obstructions entirely, while the ISO model includes only a single scaling factor to represent sheltering; both also neglect small structural elements such as roof overhangs and windowsills. Charisi and Thiis [34–36] combined the ISO standard with ray-tracing analysis to account for the sheltering effects of façades geometry, validating predicted WDR against measurements from thermal sensors and thermal imagery [36,37], as well as Computational Fluid Dynamics (CFD) simulation [35]. Beyond semi-empirical models, CFD have been validated for WDR predictions [38–41], and applied to obstructed urban façades [39,42]. Kubilay et al. [43] further integrated CFD with radiation modeling to derive spatially varying façade temperatures and relative humidities, providing a basis for defining boundary conditions for numerical hygrothermal simulations.

Despite their accuracy, CFD simulations remain rarely used in practice due to their complexity with the high level of expertise required, and substantial computational demands. These constraints limit their usability when investigating the microclimate factors that drive localized degradation or when linking microclimate to hygrothermal performance indicators. Consequently, there is a need for reliable, accessible methods that can represent microclimate variations across façades without relying on CFD modelling.

1.3. Aim and scope

This paper examines whether commonly available engineering tools can estimate microclimate variations that drive F-T degradation on brick façades, thereby providing a practical alternative to CFD-based microclimate modelling. Building on the limitations of existing deterioration models and hygrothermal performance indicators, the study explores whether microclimate-aware boundary conditions, derived from semi-empirical WDR models and detailed radiation analysis, can reconstruct the spatial distribution of degradation observed on real façades.

Section 2 reviews observational studies of hygrothermally induced deterioration, highlighting the need for simulation approaches that account for spatial microclimate variability. Section 3 describes the proposed three-phase framework, outlining the available tools and methods and defining the requirements for each phase. The framework includes: 1) microclimate modeling, combining semi-empirical wind-driven rain estimation with solar and longwave radiation analysis; 2) hygrothermal modeling, using 1D simulations to quantify the moisture and temperature response in each façade section; and 3) post-processing where freeze–thaw performance indicators are applied to estimate degradation risks in each section.

Section 4 applies the framework to a brick façade in Gothenburg, Sweden, where degradation has previously been documented across 104 sections. Two WDR models (ISO 15927-3:2009 and the Straube-Burnett (SB) model), Ladybug-derived estimates of solar irradiation and sky-view factors, and longwave radiative balance equations, are used to generate 31 years of microclimate-dependent boundary conditions for hygrothermal simulations in WUFI 2D-4. Section 5 evaluates the methodology by comparing the modelled risk patterns with the observed degradation distribution. Sections 6 and 7 discuss the findings, limitations, and implications, and present the conclusion.

2. Field studies on hygrothermal degradation

Understanding the long-term performance of façade materials under realistic exposure conditions is critical for predicting durability and ensuring structural integrity. This literature review targets studies investigating moisture-induced degradation in actual building envelopes, focusing on whether they integrate field observations with hygrothermal modeling or measurement techniques. Of particular interest is research that not only documents localized façade deterioration but also explains it through combined experimental and simulation-based approaches. This review thereby positions the present methodology within the broader context of the current research.

Most experimental field studies have focused on internally insulated brick buildings, evaluating risks of mold growth and wood decay risks at moisture-sensitive locations such as wall-insulation interfaces and embedded beam ends. Studies conducted without hygrothermal modeling [44–48] monitored interstitial conditions for 1-4 years, relying on visual inspections, spore measurements or mold growth models to evaluate moisture safety—reporting no significant degradation overall. However, Jensen et al. [47,48] demonstrated that the alkalinity of adhesive mortar influences mold development. Notably, these two studies were performed on purpose-built test walls with fully characterized material properties. In contrast, the remaining studies did not specify brick material properties, limiting the transferability of their findings.

Other studies combined field measurements with hygrothermal modeling, using calibrated simulations to predict long-term mold development in internally insulated brick walls. Work conducted in Denmark [49–51], Estonia [52] and Belgium [53] monitored interstitial temperature and humidity conditions for 9 months to 2.5 years. Material characterization varies significantly across these studies, from unspecified properties to fully laboratory-tested datasets, with some relying on database values [49,52]. Overall, the results point to elevated hygrothermal risks in internally insulated brick walls. However, the predicted mold development is highly sensitive to local boundary conditions, underscoring the importance of site-specific moisture loads and microclimate exposure.

Similar approaches have been used to examine how external insulation influences hygrothermal performance. McNally et al. [54] calibrated hygrothermal models against year-long measurements of brick-veneer wall assemblies and applied the calibrated models to assess mold sensitivity at different locations in Canada using ASHRAE Standard 160. Hietikko et al. [55] monitored timber-framed walls with brick veneer in Finland and found that thicker insulation layers increased the risk of mold development.

Degradation mechanisms beyond mold growth and wood decay are less frequently addressed in field studies. Odgaard et al. [56] combined hygrothermal monitoring with visual frost-damage inspections on insulated and uninsulated masonry spandrels in Copenhagen, Denmark, reporting no detectable deterioration after 2 year and 8 months. Johansson and Wahlgren [57] documented pronounced efflorescence and salt crystallization on interior masonry surfaces in Gothenburg, Sweden, during chamber-based exposure tests. De Andrade et al. [58] correlated twelve condition-assessment data points—each representing an entire clad façade in Brasília, Brazil—with 1D hygrothermal simulations, identifying total solar radiation, thermally induced stress, and wetting-drying cycles as the key drivers of degradation.

Some studies analyzed moisture-induced façade degradation without directly measuring or modeling hygrothermal conditions, instead correlating observed damage with WDR exposure. Lindman et al. [59] analyzed inspection records from Finnish concrete façades—including 232 cases with brick tiles—identifying WDR as the most influential factor in delayed ettringite formation and F-T damage Similarly, Pakkala et al. [60] demonstrated a significant correlation between WDR exposure and F-T damage across 472 concrete façade buildings in Finland, including a case study mapping WDR distribution across a single façade using ISO 15927-3 and comparing it with observed damage. Building on this, Pakkala et al. [61] also made a multilinear regression model to predict façade degradation on a general scale based on location and orientation. Wu et al. [62] evaluated 2,100 damage records across various façade types in Sweden, highlighting rain infiltration as the primary cause. Although neither study focuses specifically on brick masonry, both underscore WDR as a key driver of façade deterioration. Kyllingstad et al. [63] demonstrated good agreement between CFD-derived WDR mapping and observed frost damage through image analysis. Similarly, Wang and Wang [64] used calibrated CFD modeling to investigate deterioration patterns on a heritage building in Shenyang, China, finding that simulated ice formation within a wooden column is expected to cause future cracking and surface peeling.

Regarding F-T degradation—the primary focus of this study—only a single field study has combined long-term hygrothermal monitoring with simulation. Ueno et al. [65] correlated 12 years of sensor data from two brick wall assemblies in Boston with 1D hygrothermal models, assessing F-T risk by comparing modeled moisture contents 2 mm and 5 mm below the façade surface with the critical degree of moisture saturation, S_{crit}. The study references a consultant's report for material properties on the brick samples but provides limited details beyond S_{crit}. More commonly, F-T degradation is investigated in laboratory settings, either using individual material specimens [20,21,66–68], composite assemblies [19], or through the development of mechanistic ice-content models [28].

A consolidated overview of the studies described above is presented in Table 1.

In summary, the review shows that on-site investigations of moisture-related shortcomings and degradation have primarily focused on assessing mold-growth risks associated with adding internal insulation to existing buildings. These studies typically combine hygrothermal simulations with field measurements to estimate the expected performance of proposed insulation systems. Other degradation mechanisms, including F-T processes, have received less attention in field study investigations of façade assemblies. Only isolated efforts have attempted broader assessments: one study compared CFD-derived WDR exposure with observed façade degradation, while another correlated degradation across entire façades with 1D hygrothermal simulations. Freeze-thaw damage is otherwise almost exclusively examined in laboratory settings.

Notably, no study was found that a) quantifies freeze-thaw degradation across whole facades in the field, and b) models long-term heat and moisture transport within the façades assemblies to explain the localized nature of deterioration. This gap underscores the need for a methodology capable of linking long-term, full façade hygrothermal modeling to observed patterns of degradation. The methodology introduced in this paper aims to address this need by leveraging commonly available engineering tools to perform full-façade hygrothermal simulations that can be directly compared with field-observed damage.

3. Overall methodology

The proposed methodological framework structures the assessment of façade-level degradation risk into three sequential phases:

1) **Microclimate modeling:** In the first phase, the façade is divided into discrete sections within a 3D representation of the surrounding built environment. For the center point of each section, boundary conditions including solar irradiation, sky longwave radiation, and wind-driven rain (WDR), are determined using irradiation analysis tools and semi-empirical WDR models.
2) **Hygrothermal modeling:** In the second phase, the boundary conditions derived for each façade section are to a corresponding set of hygrothermal simulations. This results in a series of parallel models that describe the localized heat and moisture responses across the façade.
3) **Post-processing:** In the final phase, the hygrothermal responses are evaluated using selected performance indicators. The results are then spatially mapped to visualize the distribution and severity of degradation across the entire façade surface.

The framework does not prescribe any specific tool or method, making it adaptable to available resources and project context. The specific tools employed in this study are introduced in Section 4. Each phase consists of multiple steps, as illustrated in Fig. 1.

3.1. Microclimate modelling

Practitioners modeling microclimates without CFD face challenges in defining WDR, as obtaining measured WDR data across entire façades is

Table 1

Summary of field studies on hygrothermal performance and moisture-induced degradation.

Study type	Reference	Location / Climate	Brick Material properties	Monitoring	Hygrothermal Modeling	Spatial scope	Degradation / assessment
Internally insulated systems – mold/decay risk							
Without modeling	Toman et al. [44]	Prague, CZ	Unspecified	4 years	None	Multiple heights, 2 orient.	No condensation observed
	Morelli & Møller [45]	Folehaven, DK	Unspecified	2 years	None	Multiple points, different orient.	No degradation
	Harrestrup & Svendsen [46]	Copenhagen, DK	Unspecified	1 year	None	Beam ends, 2 orient.	No degradation
	Jensen et al. [47, 48]	Denmark (coastal)	Known	2.5 years	None	Interface, 24 test walls	Mold growth observed
With modeling	Hansen et al. [49]	Copenhagen & Haderslev, DK	Approx. from database	2.5 years	Calibrated, 10-yr sim.	Beam ends + interface	No degradation + mould growth index
	Pagoni et al. [50]	Copenhagen, DK	Lab-tested	20 months	Calibrated	Single point, 2 orient.	No degradation observed
	Jensen et al. [51]	Lyngby, DK	Lab-tested	2-4 years	Calibrated + future climate scenarios	Wall to ceiling connection, four insulation systems, 7 points	Increased relative humidity in critical locations
	Klõšeiko et al. [52]	Estonia	Database + adjusted based on lab tests	Chamber test 9 months	Calibrated	Interstitial points	No degradation
	Dang et al. [53]	Leuven, BE	Known (Vandersanden ® Robusta brick)	1 year	Calibrated + future climate scenarios	Multiple points in three test assemblies	No degradation observed
Externally insulated systems – mold risk							
	McNally et al. [54]	Ottawa, CA	Experimentally determined	1 year	Calibrated	Single assembly	No degradation observed
	Hietikko et al. [55]	Tampere, FI	Based on manufacturers and literature	1 year	None	4 wall types	No degradation observed
Other degradation mechanisms (field)							
Frost + mold inspection	Odgaard et al. [56]	Copenhagen, DK	Unspecified	2 yr 8 mo	None	2 brick spandrels, 4 points	No observed degradation
Salt crystallization	Johansson & Wahlgren [57]	Gothenburg, SE	Unspecified	1 yr 8 mo	None	Single wall, 10 points	Observed salt crystallization in brick mortar
Facade-scale correlation	De Andrade et al. [58]	Brasília, BR	Not listed	None, using preexisting degradation data	1D model, 3 years	12 facades (1 pt each)	Correlates degradation to hygrothermal modeling outcomes
Wind-driven rain (WDR) based analysis							
	Lindman et al. [59]	Finland	N/A,	Database analysis (232 records of brick tile cladding)	None	Statistical	Concrete façade degradation data, Brick cladding => concrete more susceptible to damage
	Pakkala et al. [60, 61]	Finland	N/A	Database (472 records)	None	Statistical / single building	Correlates WDR with frost damage
	Wu et al. [62]	Sweden	N/A	Database (2100 records)	None	Statistical	Degradation of brick facades not specifically quantified
	Kyllingstad et al. [63]	Norway	N/A	Photo analysis	CFD (WDR)	Single building	Correlates WDR with frost damage via picture analysis
	Wang & Wang [64]	Shenyang, CN	N/A	T, RH, wind	CFD + ice sim.	Single building	No degradation was quantified
Freeze-thaw (field + modeling)							
	Ueno et al. [65]	Boston, USA	S_{crit} only; other characteristics not listed	12 years	1D (2–5 mm depth)	2 assemblies, 2 orient.	No degradation was quantified

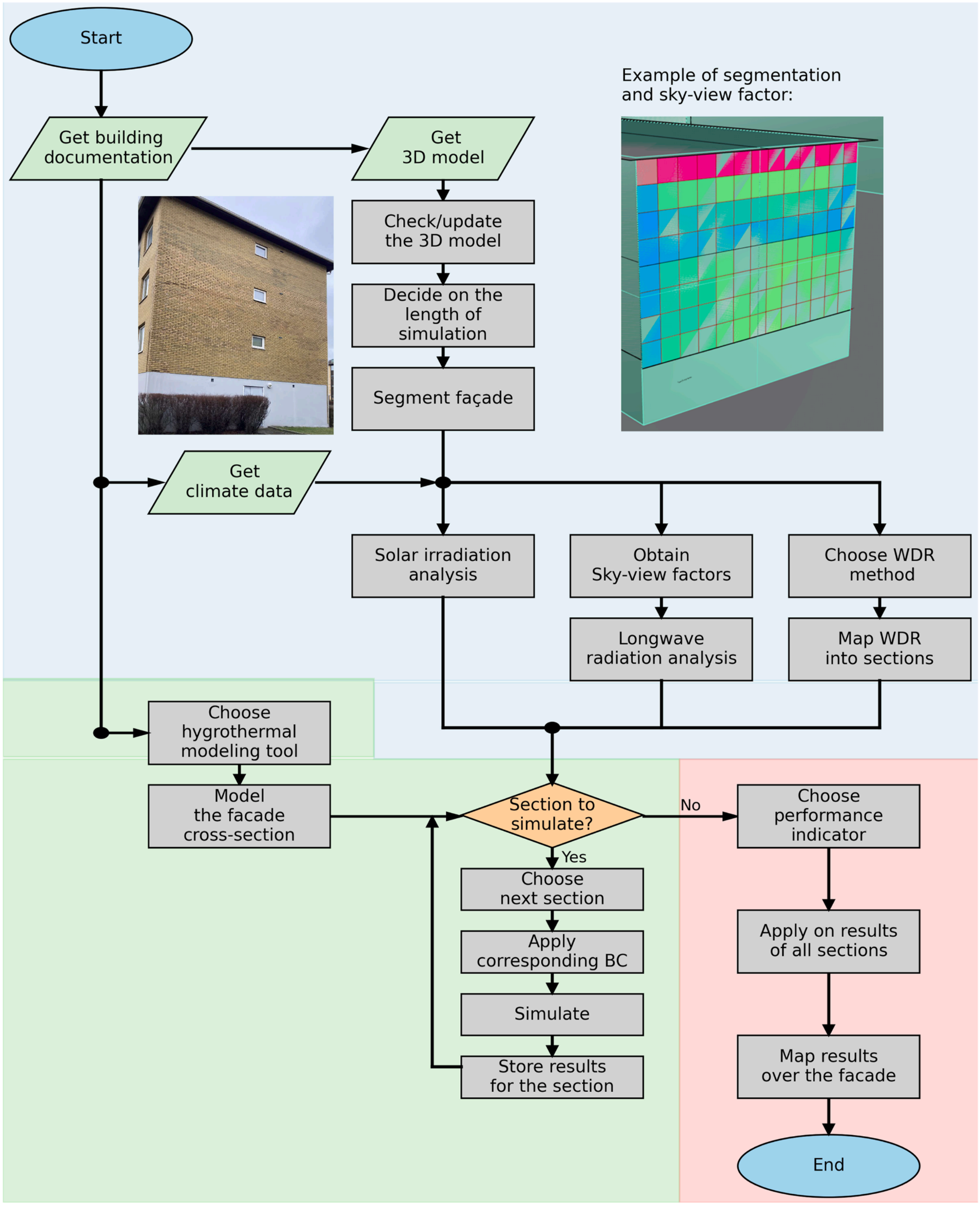

Fig. 1. Overview of the phases in the proposed methodological framework for assessing the moisture-induced degradation risk across a façade. Background colors distinguish its phases: blue for 1) Microclimate Modeling, defining façade sections and localized boundary conditions; green for 2) Hygrothermal Modeling, quantifying section-specific heat and moisture responses; and red for 3) Post-processing, where performance indicators are evaluated and degradation risks are mapped across the façade.

labor-intensive and rarely feasible. The approach adopted here combines detailed irradiation analysis with semi-empirical WDR models, balancing computational efficiency with sufficient physical representation of microclimatic loads.

The framework requires: 1) a three-dimensional model of the façade and its surrounding built environment, verified against technical drawings; 2) building documentation; and 3) hourly climate data, which may represent measured or projected conditions.

Tools like Ladybug [30] and De Luminae [31] can perform irradiation analysis and calculate sky-view factors (g_{atm} [-]) across meshed façade sections. Such software typically combines the effects of direct and diffuse solar radiation, but disregards solar radiation reflected by the surroundings. This may be integrated into solar analysis outputs using the following expression:

$$I_s = I_{s,modeled} + g_{terr} \times I_{s,refl} = I_{s,dir} + g_{atm} \times I_{s,diff} + g_{terr} \times I_{s,refl} \tag{1}$$

$$I_{s,refl} = \rho_{s,terr} \times \left(I_{s,dir,\ h} + I_{s,diff}\right) \tag{2}$$

Where $I_{s,modeled}$ [W/m^2] is the modeled output from the solar irradiation analysis comprising the incidence of direct $I_{s,dir}$ [W/m^2] and diffuse $I_{s,diff}$ [W/m^2] solar irradiation on a façade section, g_{terr} [-] is the terrestrial view factor calculated as $1 - g_{atm}$, $I_{s,refl}$ [W/m^2] is the solar radiation reflected by the surrounding, $\rho_{s,terr}$ [-] is the short-wave reflectivity of the ground. $I_{s,dir,h}$ [W/m^2] is the direct horizontal solar radiation. Longwave radiation for each façade section can be estimated through a radiative balance equation:

$$I_l = g_{atm} \times I_{l,atm} + g_{terr} \times (I_{l,terr} + I_{l,refl}) \tag{3}$$

Where $I_{l,atm}$ [W/m^2] is the atmospheric counter-radiation obtained from climate data, g_{atm} [-] is the sky-view factor obtained from irradiation analysis, Ground-reflected radiation $I_{l,refl}$ [W/m^2] and terrestrial counter-radiation $I_{l,terr}$ [W/m^2] can be calculated using following equations:

$$I_{l,refl} = \rho_{l,terr} \times I_{l,atm} \tag{4}$$

$$I_{l,terr} = \epsilon_{l,terr} \times \sigma \times T_{surr}^4 \tag{5}$$

Where $\rho_{l,terr}$ [-] is the long-wave reflectivity of the ground, $\epsilon_{l,terr}$ [-] is the long-wave emissivity of the ground, σ [W/m^{2}K^4] is the Stephan-Boltzmann constant and T_{surr} [K] is the temperature of the surrounding surfaces. For simplicity one can assume the surrounding surfaces to behave as opaque grey bodies with the air temperature.

Any semi-empirical approach for WDR quantification, including ISO 15927-3:2009 or Straube-Burnett (SB) model, can be leveraged to map WDR across meshed façade sections, with model selection depending on their respective limitations. The ISO standard accounts for terrain type, topography and distance to the nearest obstruction but it provides only a coarse distinction of WDR across six façade geometries. The SB model offers detailed mappings for three façade geometries, allowing for fine differentiation of incoming WDR, while simplifying other exposure factors.

3.2. Hygrothermal modelling

The boundary conditions for each façade section are applied in a corresponding set of hygrothermal models. Any hygrothermal simulation model validated according to EN 15026:2023 is acceptable, provided it accounts for the latent heat of fusion to capture a gradual change in the phases of water—necessary for accurate F-T modeling.

Since façade sections are modeled independently, one-dimensional approaches are both logical and computationally efficient. A grid sensitivity test should be performed following EN 15026:2003, which recommends comparing results from normal and refined grids—typically with finer discretization near boundaries. The differences between grid variants shall be within acceptable tolerances (< 1K for temperatures and $< 5\%$ for relative humidities); if exceeded further refinement is needed. It is also recommended to verify that moisture from rain does not remain located in grid cells near the surface, as this indicates inadequate meshing.

Material parameters such as thermal conductivity, porosity, and sorption isotherms govern the hygrothermal response and can be determined through laboratory testing. While this yields the most accurate material data, it often necessitates destructive sampling which may not be possible. Therefore, material parameters may be approximated using databases or available literature.

3.3. Post-processing

The risk of physical degradation in cold climate façades is often linked to freezing and thawing. Performance indicators for F-T risks generally fall into two categories: 1) indicators that estimate the presence of ice indirectly, and 2) indicators that quantify ice volume directly.

Indicators based on direct ice volume rely on the critical degree of saturation (S_{crit}), a threshold above which bricks dilate upon freezing, as defined by Fagerlund [69] and later investigated by Mensinga [26]. The most widely used indicator is the number of F-T cycles, counting instances when material temperature falls below freezing while moisture content exceeds S_{crit}. The freezing temperature may be set at 0°C or lower, depending on pore structure and freezing point depression. DIN 4108-3 (2018), for example, specifies -5°C. Kočí [70] describes additional indicators including the Modified Winter Index (rate of exceeding critical conditions), the Number of Indicative F-T Cycles (cycles lasting at least 2 hours), Time-of-Frost (annual time exceeding critical levels), and Amount-of-Frozen-Water (total annual ice content).

Indicators based on direct estimation of ice volume use explicitly modeled ice formation as the basis for risk estimates. The hygrothermal software DELPHIN includes such an indicator, counting F-T cycles according to user-defined thresholds for the rate of ice formation by volume. The Freeze-Thaw Damage Risk (FTDR) index, developed by Zhou [28], avoids integer cycle counting by accumulating the difference between the maximum and minimum ice content saturation degree in each complete or incomplete F-T cycle, neglecting variations below a threshold value of 0.05.

4. Methodology implementation / case study

The Flatås area, located in Gothenburg, Sweden, is a residential neighborhood developed in a consistent architectural style during the 1960s. It consists of mid-rise, multi-family buildings with both ventilated and unventilated brick façades, many of which have not been renovated and show clear signs of degradation due to freezing and thawing. These characteristics make the area a valuable case study for assessing and comparing the proposed framework. A previous study assessed degradation patterns on 16 façades using drone imagery and computer vision [71], from which the most damaged façade is selected for the purpose to showcase the proposed methodology. Fig. 2 presents a photograph of the case study façade and a heatmap spalling prevalence across it, generated by dividing the brickwork into 104 sections, each analyzed using a pre-trained YOLOv4 algorithm to estimate degradation ratio—the fraction of the damaged to total bricks per section—verified through manual inspection. Observations were conducted in spring of 2024. For later comparison with modeled risk estimates, the degradation ratio of each section (varying between 0 and 0.9) was normalized by the maximum observed value across the façade, yielding values between 0 and 1.

According to documentation from 1965, the façade is 13.5 m wide and 11.5 m high, with 0.7 m roof overhang. The wall consists of a rendered lightweight concrete wall up to 2.8 m above the ground, topped by an outer layer of yellow brickwork spanning the remaining height. The spalling distribution forms a clear pattern: a strip of elevated degradation spans the façade width (rows 2 and 3); low to no degradation appears beneath the roof overhang (rows 0 and 1) and near the bottom right corner; and the brickwork is generally more damaged on the left side. The highest degradation ratios are concentrated near the right corner within row 3, peaking at column 12.

This pattern likely stems from the surrounding building's influence on the façade's microclimate. The façade faces south with a 6° westward tilt, sheltered from south and east by a building 14.5 m away, while another 35 m to the west leaves a gap towards the southwest, obstructed only by grown trees. The study site is located in a suburban area with flat surrounding terrain. These site characteristics informed the selection of input parameters for the semi-empirical WDR models, as described in Section 4.1.

4.1. Generating local boundary conditions

Hourly weather data for Gothenburg, Sweden, covering 1991 to 2021, were obtained from a validated climate dataset generated under the A1B emission scenario. The dataset is based on a regional climate model RCA3, driven by the global climate model ECHAM5 and provided by the Swedish Meteorological and Hydrological Institute (SMHI) [72]. Modeled climate data were preferred over measured data for their accessibility and completeness. Fig. 3 summarizes the climate conditions

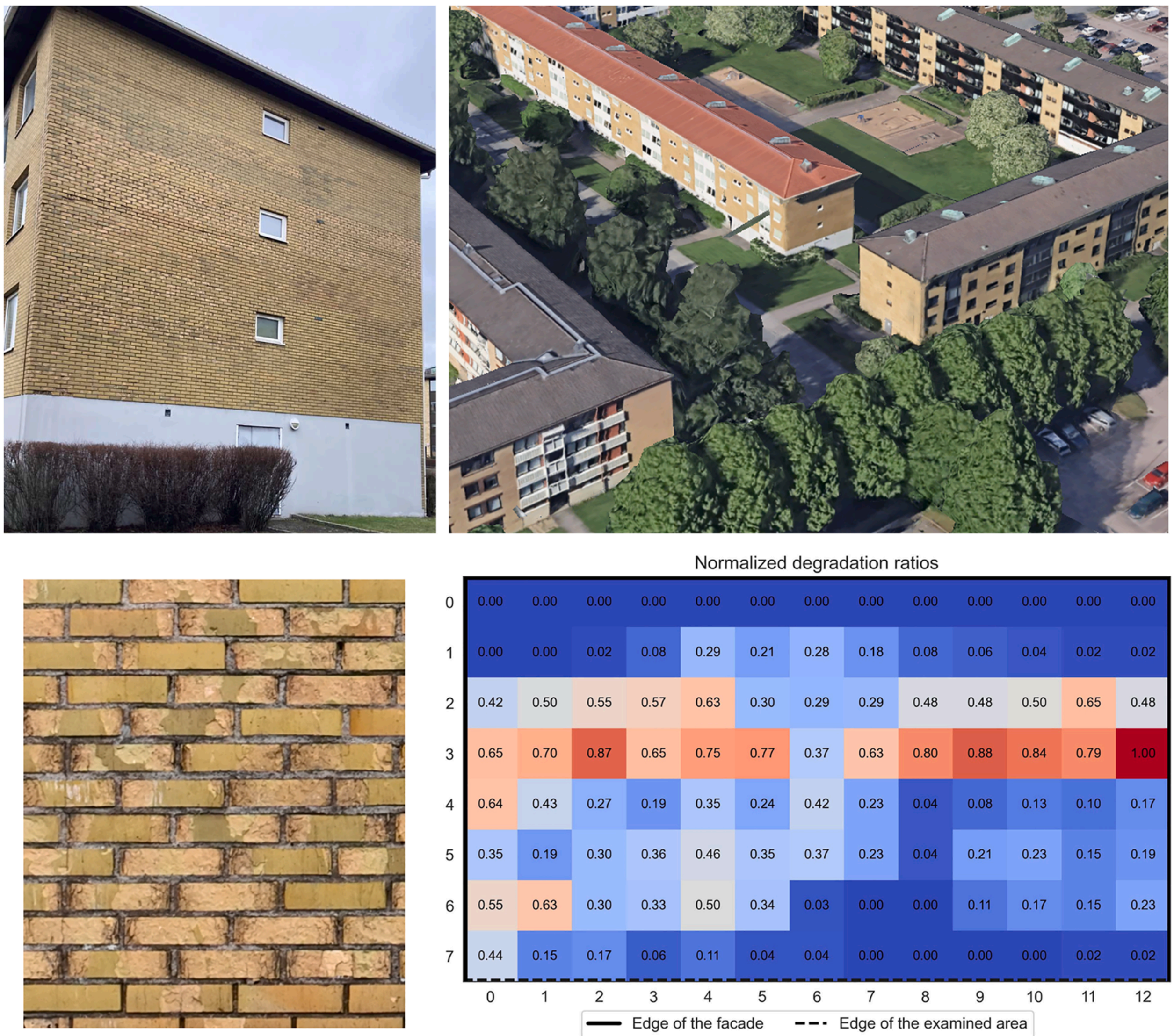

Fig. 2. Summary of the case study façade. Top left: photograph of the façade. Top right: view of the surrounding context. Bottom left: close-up detail of a façade section. Bottom right: heatmap obtained by computer vision assessment, illustrating the division of the façade, with degradation ratios indicated for each [71]. The axes represent section indices (column and row numbers).

as monthly means and standard deviations over the 31-year period. Table 2 shows the means and ranges of all climate variables over the same period.

A three-dimensional model of the neighborhood was obtained from the Digital Twin City Centre (DTCC) model [73]. Façade dimensions were verified against technical documentation and supplemented with field measurements where available. Roof geometries, including overhangs, were added to ensure accurate shading representation. Irradiation analysis using the Ladybug tool divided the façade into 104 sections corresponding to the degradation data. Modeled irradiation was complemented by solar radiation reflected by the surrounding estimates using Eqs. (1) and (2), assuming the short-wave reflectivity of the ground equal to 0.2. Obtained sky-view factors were used to calculate incident longwave radiation at the center of each section, using Eqs. (3-5) and assuming longwave reflectivity and emissivity of surrounding equal of 0.1 and 0.9, respectively.

WDR exposure was quantified using both ISO 15927-3:2009 and the SB model. For the ISO model, the wall factor was set to 0.4 for all façade sections, corresponding to the "three-storey wall with eaves" in Table 4 of the standard. Although the case study façade has four above-ground storeys, the standard does not provide a more appropriate case for determining the wall factors. The site's suburban setting and flat surrounding terrain correspond to a Category III roughness classification and a topography coefficient of 1. An obstruction coefficient 0.3 was estimated based on the sheltering building located 14.5 m to the south. For the SB model, none of the provided RAF coefficient mappings matched the case study façade; therefore, the "tall building" scenario was selected, as the façade height exceeds 10 m. Table 3 summarizes the scaling factors applied in both models to generate 31-year hourly WDR boundary conditions for all façade sections.

The hourly WDR intensities from both models were each combined with the modeled solar irradiation and longwave radiation, both modeled by Eqs. (1-5), using custom made Python script, generating two sets of microclimate boundary conditions for each of the 104 façade sections. The datasets were supplemented by hourly air temperature, relative humidity, wind direction and wind speed, with wind speed corrected by height using the roughness coefficient (ISO model) or the power law function (SB model). WDR, solar irradiation, and longwave radiation were passed to WUFI as directly measured variables, ensuring that these microclimate-derived inputs are used without further preprocessing by the program.

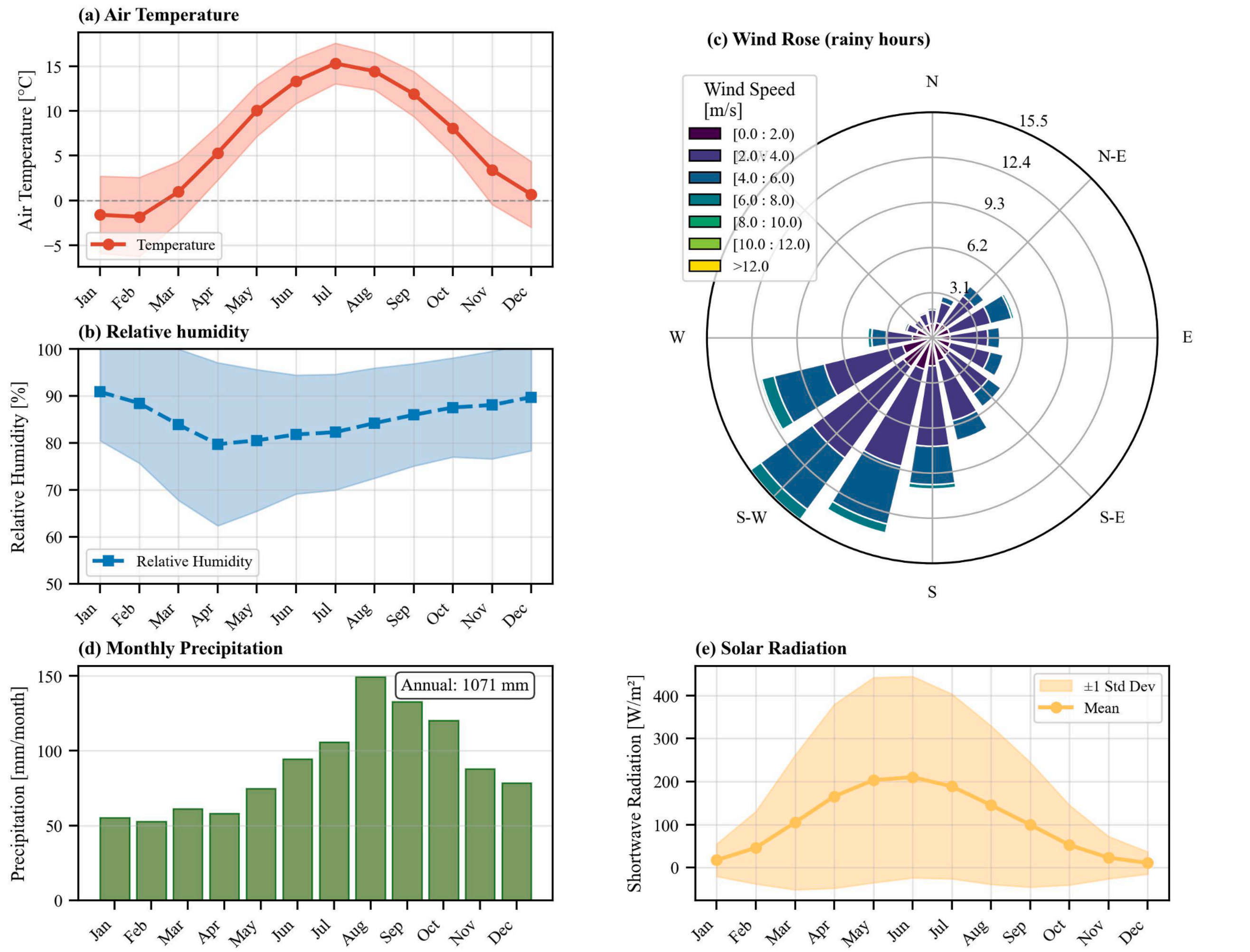

Fig. 3. Climate conditions for Gothenburg, Sweden (1991–2021) using the A1B scenario: (a) monthly air temperature (b) monthly relative humidity, (c) wind rose during rainy hours, (d) monthly precipitation, (e) shortwave radiation. Shaded areas indicate ±1 standard deviation.

Table 2
Summary of used climate conditions for Gothenburg, Sweden (1991–2021) using the A1B scenario.

Parameter	Mean	Range
Air temperature	6.7°C	-23.4 to 25.1°C
Relative humidity	85.3%	27.4 to 100.0 %
Annual Precipitation	1071 mm/year	655 to 1356 mm/year
Wind speed	2.9 m/s	0.0 to 11.4 m/s
Solar radiation	105.8 W/m2	0.0 to 863.2 W/m2

4.2. Material selection and hygrothermal modeling set-up

According to the technical documentation, the façade consists of a 108 mm outer layer of yellow extruded bricks and 200 mm of aerated concrete. As material properties are unspecified, two brick types are analyzed to assess how different outer layer properties influence the spatial distribution of subsurface degradation risk. The first set-up uses WUFI's "*Solid Brick, extruded*" as the outer layer—believed to be the closest match to the façade brick—and "*Aerated Concrete (Density: 600 kg/m³)*" as the inner layer. The second set-up uses "*Solid Brick ZO*" as the outer layer, selected for its markedly different hygrothermal parameters. Table 4 summarizes the material data, complemented by Fig. 4 showing

Table 3
Summary of scaling factors for WDR models employed.

ISO standard model			SB model		
$R_{wdr} = \frac{2}{9} \cdot C_R \cdot C_T \cdot O \cdot W \cdot U_{10} \cdot R_h^{0.88} \cdot \cos\theta$			$R_{wdr} = DRF \cdot RAF \cdot U(z) \cdot R_h \cdot \cos\theta$		
	Values	Ref. in ISO		Values	Ref.
C_R - roughness coefficient			**U(z) – power law function**		
$C_R(z) = K_R \cdot \ln\left(\frac{z}{z_0}\right)$ *for* $z \geq z_{min}$	$K_R = 0.22$ $z_{min} = 8m$	Table 1 (Cat. III)	$U(z) = (z/10)^{\beta}$ β - Power law coefficient	 0.22	 [74]
$C_R(z) = C_R(z_{min})$ *for* $z \geq z_{min}$			**DRF - Driving Rain Factor**	V_T Based on [75,76]	
C_T - topography coefficient	1		$DRF = 1/V_T$		
O - Obstruction coefficient	0.4	Table 3 (15 m)	**RAF - Rain Admittance Factor**	0.4-1.02	[77] Table 4 - "Tall Building "
W - Wall factor	0.4	Table 4			

Table 4
Summary of material data used in the case study [78].

	Bulk density	Porosity	Spec. Heat Capacity	Thermal conductivity	Water Vapor Diffusion Resistance factor	Free water saturation
	kg/m^3	m^3/m^3	J/kgK	W/mK	-	kg/m^3
Solid Brick, extruded	1650	0.41	850	0.6	9.5	370
Solid Brick ZO	1873	0.29	823	0.91	45	126
Aerated concrete (Density: 600 kg/ m^3)	600	0.72	850	0.14	8.3	470

the moisture sorption isotherms of the three materials.

The façade's hygrothermal response is modeled in WUFI 2D-4 using a one-dimensional model representation for each façade section. Initial conditions assume outdoor temperature and relative humidity corresponding to January 1991 monthly means (T = 1.75°C, RH = 89%) for the outer layer, with T = 15°C for the inner layer. The outer surface heat transfer coefficient is wind-dependent, while 8 W/m^2K is assumed for the inner surface. Moisture from wind-driven rain were applied at the exterior surface only, with a Rain Water Absorption factor of 0.7. Air exchange rates and internal moisture sources were not considered. Indoor boundary conditions follow the "Medium Moisture Load" defined in EN 15026.

A grid sensitivity test compared WUFI's automatic meshing options (coarse, medium, fine) and five additional manually defined meshes derived from the fine mesh, with grid cells increased by 10 per iteration. Moisture content and relative humidity at 5 mm depth were monitored, using the finest mesh as reference. Three-year simulation using boundary conditions for a randomly selected façade section confirmed that the wetting front propagates throughout the entire brick layer, indicating no numerically induced resistances from mesh discretization or hydraulic resistance averaging [79]. Table 5 summarizes the results, including the mean absolute error (MAE) and the maximum moisture content and RH error during the last winter season, measured against the finest mesh.

As observed, MAE is low across all examined meshes, though maximum RH and moisture content differences vary notably between options. For instance, mesh "Fine" exhibited a 3.3% maximum RH deviation from the finest mesh, whereas mesh "Fine3" showed only a 0.7%, corresponding to 18.1 and 4.1 kg/m^3 of moisture content, respectively. "Fine3" is therefore adopted for the case study. Fig. 5 shows a schematic cross-section of the modeled wall with its "Fine3" mesh discretization.

4.3. Performance indicators

Two performance indicators quantify F-T degradation risk across the 104 façade sections: the number of F-T cycle, and the FTDR index. The first material set-up— extruded bricks—is analyzed using both indicators. Given uncertainty surrounding S_{crit}, the F-T cycle analysis is performed iteratively, incrementing the RH threshold by 5% 20%, reducing to 1% after 95% RH threshold. In this paper, a freeze-thaw cycle is counted when RH exceeds the threshold and temperature simultaneously drops below 0°C, evaluated at a depth of 5 mm beneath the outer surface. This depth was selected to capture the hygrothermal conditions close to the exterior surface, where the spalling damage manifests on the façade. A freezing threshold of 0°C is adopted as a conservative assumption, consistent with the engineering focus of the proposed methodology.

The FTDR index requires ice content by volume rather than an RH threshold. As it is not directly provided in WUFI's result files, WUFI internally approximates ice content during freezing using the freezing limit potential [80], expressed as:

$$w_{ice}(T, w_{tot}) = \max\left(0, w_{tot} - w\left(\varphi_f(T)\right)\right) \quad (6)$$

$$\varphi_f(T) = 1 + 0.01 \times T \quad (7)$$

where T (°C) is temperature, w_{tot} (kg/m^3) is total moisture content, w (ϕ_f) (kg/m^3) is equilibrium water content, φ_f (-) is equilibrium RH potential and w_{ice} (kg/m^3) is ice content. This differs from more rigorous approaches in DELPHIN and [28], which compute ice content directly; FTDR results obtained using WUFI should therefore be interpreted accordingly.

Both indicators estimate cumulative degradation risk across all façade sections over 31-year period. Risk estimates are mapped onto the façade sections and compared with the observed degradation using Pearsons's correlation coefficient (PCC).

5. Results

The results are presented in two main parts. Section 5.1 reports detailed outcomes for the material case with *Solid brick, extruded* as the outer layer, including hygrothermal performance time series, spatial mapping of F–T cycles and FTDR indices, and their comparison with observed degradation. Section 5.2 presents a reduced analysis for the

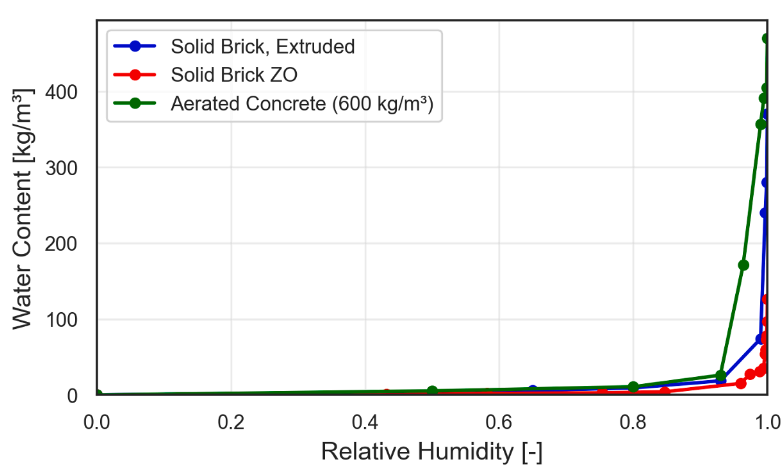

Fig. 4. Moisture sorption isotherms for materials used [78].

Table 5
Summary of the grid sensitivity test showing the number of elements used for each material layer and the corresponding expansion factors. The performance of each mesh is measured using MAE and the absolute maximum RH error derived from the final winter season of the three-year period under investigation. The meshes are compared against the fines mesh "Fine6".

	Number of elements				Expansion Factor	MAE [%]	Maximum difference	
	Brick layer left side	Brick layer right side	AEC left side	AEC right side			RH [%]	W_c [kg/m^3]
Coarse	19	15	20	21	0.9090-1.1001	0.078	6.5	37.0
Medium	28	24	30	30	0.9081-1.1012	0.048	3.1	16.9
Fine	38	30	41	41	0.9530-1.0493	0.042	3.3	18.1
Fine2	50	50	51	51	0.9530-1.0493	0.030	1.4	14.1
Fine3	60	60	60	60	0.9530-1.0493	0.006	0.7	4.1
Fine4	70	70	70	70	0.9530-1.0493	0.003	0.4	5.0
Fine5	80	80	80	80	0.9530-1.0493	0.001	0.2	5.0
Fine6	90	90	90	90	0.9530-1.0493	-	-	-

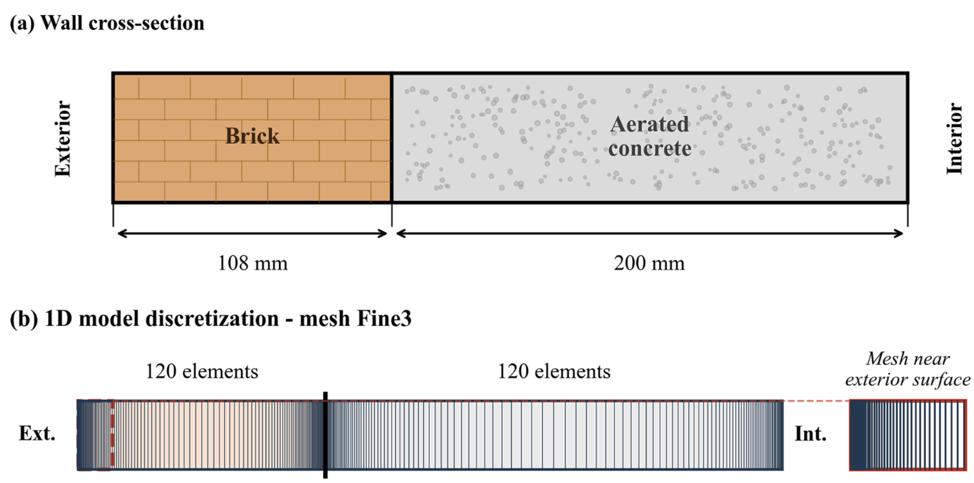

Fig. 5. (a) Schematic cross-section of the wall. (b) 1D model discretization using "Fine3" mesh.

case with *Solid Brick ZO* as the outer layer, focusing on the F-T cycle mappings and sensitivity to material assumptions.

5.1. Results for Solid brick, extruded as an outer layer

5.1.1. Hygrothermal performance of representative sections

To illustrate differences in hygrothermal performance across the façade, results for two out of 104 differently located points are presented. Point A is situated at the top left corner of the façade, near the roof overhang, while Point B is in its middle of the façade, unobstructed by architectural elements. Fig. 6 shows the location of the two points and highlights their microclimate exposure.

Despite the roof overhang, Point A represents the most exposed façade section both in terms of WDR (SB model; RAF = 1.02) and the average incoming solar irradiation during wintertime (90 kW/m^2). Nevertheless, its sky-view factor is among the lowest on the façade (22%). Point B exhibits a close to average sky-view factor (37%) and the average solar irradiation (65 kW/m^2). In the context of the SB model, Point B can be regarded as the opposite extreme to Point A with one of the lowest WDR exposures (RAF = 0.4). It should be noted that both points are identical in terms of their Wall factors as defined by the ISO standard.

Fig. 7 shows the hygrothermal performance of the two points for the two WDR models at 5 mm behind the façade surface, from January to March of 1995. The simulation was initialized in 1991 and ran continuously. The year 1995 was selected as representative because its winter mean temperature is closest to the 31-year average, and the four-year initialization period ensured that built-in moisture effects had dissipated.

As illustrated, both points follow similar temperature patterns, with Point A being generally warmer. This is attributed to the roof overhang, which shelters Point A from night sky cooling while allowing direct solar radiation during winter months. Moisture content also influences the temperature fluctuations: higher moisture leads to higher thermal conductivity and heat capacity, reducing temperature rise, while greater moisture availability dampens temperature drops during freezing through latent heat release. Consequently, temperature fluctuations are more pronounced in the ISO model results, where points are significantly drier than their SB counterparts, affecting F-T cycle counts. During the examined period, Point A underwent 25 and 33 cycles, while Point B underwent 15 and 33 cycles for the SB and ISO models, respectively. Minimum temperatures were recorded near the end of the period, with the SB model exhibiting -7.9 and -12.1°C and the ISO models -14.0 and -14.9°C for Points A and B, respectively.

Regarding relative humidity, the SB model resulted in significant wetting at both points, exceeding the hygroscopic region of the moisture sorption isotherm. Moisture contents ranged from saturation in Point A (370 kg/m^3) to substantially lower moisture levels in Point B (28.5 kg/m^3), with minimal RH variation. The lowest values were 99.1% (Point A) and 94.1% (Point B). Conversely, the ISO model produced lower moisture contents, allowing greater RH variation. During the first two weeks, RH at both points fluctuated around 96.5%, after which levels diverged, with Point B consistently showing higher saturation. Minimum RH was 72.7% at Point B and 50.4% at Point A. For further illustration of hygrothermal performance, Fig. 8 shows the moisture flux and cumulative moisture balance at Points A and B for the period 1-8 January 1995, computed over the full brick layer depth and counted from the start of the year.

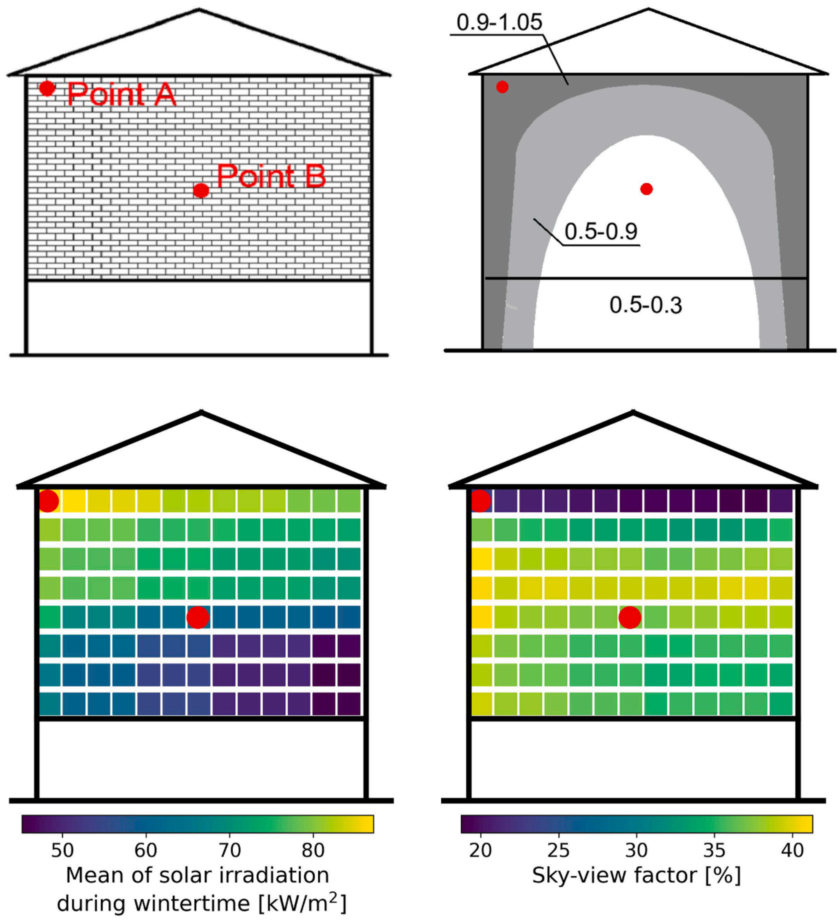

Fig. 6. Points of interest on the façade and their microclimate exposure: (top left) location of points, (top right) RAF coefficient from the SB model, (bottom left) mean of solar irradiation during wintertime, (bottom right) sky view factor.

5.1.2. Freeze-thaw cycle analysis

5.1.2.1. Results based on the ISO model. Fig. 9 shows the outcomes of the F-T cycle analysis for the ISO case, mapping the number of cycles across the façade and for 6 different RH thresholds.

As illustrated, the number and distribution of F-T cycles vary with RH thresholds, with higher thresholds resulting in fewer cycles. For thresholds from 70% to 80% (heatmaps on the top), the highest cycle counts appear on the left edge (column 0), decreasing progressively to the right. A strip spanning the façade width (rows 1-4) maintains high cycle counts, becoming more pronounced at RH 80% as sections near the roof overhang (row 0) are less exposed to sky cooling. The bottom right corner exhibits the lowest cycle count.

Increasing the threshold further reduces both the frequency and distribution of F-T cycles (heatmaps in the middle of Fig. 9). Here, the least exposed sections are directly below the roof overhang (row 0). The effect of the roof overhang is especially notable at RH 85% and 90% as the remaining area of the façade is significantly more exposed, with the bottom left corner exhibiting the highest cycle counts. At RH 95%, cycle counts decrease across the façade, with the bottom right corner becoming the area of highest risk and the roof overhang effect becoming less. For RH thresholds above 95%, no F-T cycles occur across the façade.

5.1.2.2. Results based on the SB model. Fig. 10 shows the threshold-sensitive mapping of F-T cycles across the façade using the SB model.

As illustrated, the resulting mappings are evidently influenced by the oval-shaped distribution of the rain admittance factor (RAF in Fig. 6). At the 70% RH threshold, the shape clearly protrudes, with the highest risk degradation at the center, and areas of lowest risk at the bottom right corner. As the RH threshold increases, this pattern gradually diminishes as the area of the highest risk moves towards the top left corner, dissolving completely at RH 90% and 95%. At these thresholds, the highest risk of degradation is located on the left edge (column 0), diminishing towards the right. This reduction is more pronounced in rows 5-7 with the least exposed area at the bottom right corner. Sections in rows 0-4 remain exposed to higher number of F-T cycles from left to right, resembling the strip described in the ISO model. Unlike the ISO case, no evident effect of the roof overhang is observed on the F-T exposure of the adjacent sections. Increasing the RH threshold past 95% resurface and further pronounce the oval-shaped RAF mapping; however, the center of the façade becomes the area with the fewest F-T cycles.

5.1.2.3. Comparison between ISO and SB WDR models. Fig. 11 summarizes the outcomes of the critical relative humidity threshold analysis for WDR models (minimums, maximums, average, standard deviation F-T cycles in each case). This summary includes a comparison between the simulated patterns and the observed degradation pattern on the façade as shown in Fig. 2 using PCC. The results are provided for thresholds from 50% to 95% in 5% increments, followed by 1% increments up to a 99% threshold.

The ISO model exhibits more F-T cycles in lower thresholds despite lower incoming rain intensity. At the 50% RH threshold, the façade-averaged exposure was 1660 cycles, ranging from 1375 to 1915. The SB model resulted in milder exposure, averaging 1200 cycles and ranging from 850 and 1422. This dynamic shifts at higher thresholds. While both cases exhibit fewer cycles with each increment, the drop is significantly

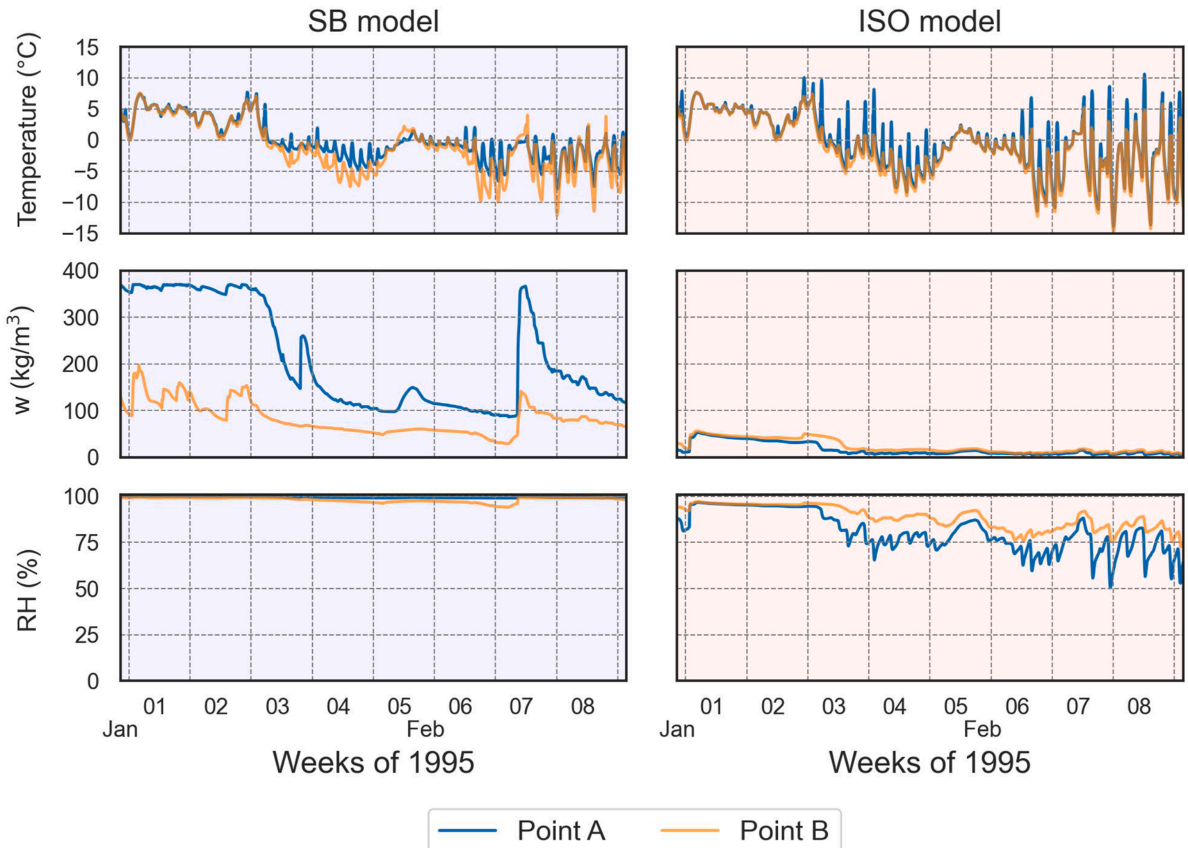

Fig. 7. Hygrothermal performance 5 mm behind the outer surface in Point A and B over the first two months of 1995. Graphs on the left show the SB case. On the right, the ISO case. The top graphs show temperatures, the middle moisture content and the bottom relative humidity.

more pronounced in the ISO case, with averages converging at 1162 and 1167 at the 80% threshold for the ISO and SB models, respectively. At the 96% RH threshold, the ISO model averages 80 cycles (ranging from 17 to 138), significantly fewer than the SB model, which averages 1075 cycles (ranging from 859 and 1283). Beyond 96%, ISO cycle counts continue to drop steadily, averaging values 11, 2, 1 at 97%, 98% and 99%, while SB model averages remain high at 1011, 895 and 800 cycles, respectively.

PCC in neither case exceeded a value of 0.75, which would indicate strong correlation of the risk mappings to the observed degradation (Fig. 2). Nevertheless, the ISO model with fixed rain intensities across the façade performed notably better, particularly at lower thresholds, peaking at the 75% RH threshold with a PCC of 0.60, after which the correlation gradually decreases. At RH thresholds above 96%, the ISO model produced near-zero F-T cycles across all façade sections, resulting in negligible spatial variance and an undefined PCC, which therefore excluded from the analysis. The SB model correlations remain low (PCC = 0.16) at the lower end of the RH threshold spectrum before increasing gradually from 70% RH, peaking at 90% with PCC of 0.32, indicating a weak correlation. To exemplify the accuracy of the best performing models, Fig. 12 provides a visual insight into how well the modeled risk aligns with real-world deterioration pattern.

Rescaling the F-T risk colormap so each case covers only its own cycle range significantly pronounces the modeled patterns. Both cases exhibit similarities and differences relative to each other and to the observed degradation. Notably, the SB model follows the same pattern as the ISO model but lacks the area of lower degradation risk beneath the roof overhang—also observable on the actual façade. Furthermore, both cases replicate the strip of degradation spanning the façade width (rows 2-4), the increased risk of degradation near the left edge of the façade and the area of low risk near the bottom right corner.

Nevertheless, the scatter plots in Fig. 12 imply that both models generally overestimate degradation risks. In both cases, the maximum risk is situated on the left edge (column 0), while the highest degradation observed is located on the opposite side (column 12), with risk estimates decreasing progressively to the right—also observable in the degradation mapping, particularly in rows 4-7. However, the rate of decreases diverges, particularly in the ISO model, where the risk shifts are more punctual. Additionally, rows 2-3 diverge with elevated degradation concentrated near the edges and lower damage at the center. While these discrepancies may not strongly affect pattern similarity, they contribute to the general risk overestimation across the façade.

The spatial analysis above only indicates where the degradation is more likely, not the absolute risk levels. Both cases in Fig. 12 show over 800 F-T cycles in their least strained areas over the 31 years, yet parts of the actual façade (i.e., beneath the roof overhang) remain undamaged, suggesting absolute cycle counts are overestimated. The analysis is therefore deepened using a dose-response function (FTDR index) to gain insights into the ice formation within the façade.

5.1.3. *FTDR index analysis*

The application of the FTDR index to the simulation results yields a distinctive interpretation of risks across the façade sections. By zooming into the representative year of 1995 and utilizing the two points (Point A and Point B from Fig. 6) to illustrate estimated ice formation and the cumulation of the FTDR index, it can be determined that there is no ice formation in the ISO model. Fig. 13 illustrates the saturation degree of ice content and the corresponding FTDR index for the SB case.

As illustrated in the two-week period of January 1995, the formation of ice is more frequent and severe in Point A. Point A exhibited 11 complete and 4 incomplete cycles, an average saturation degree of ice

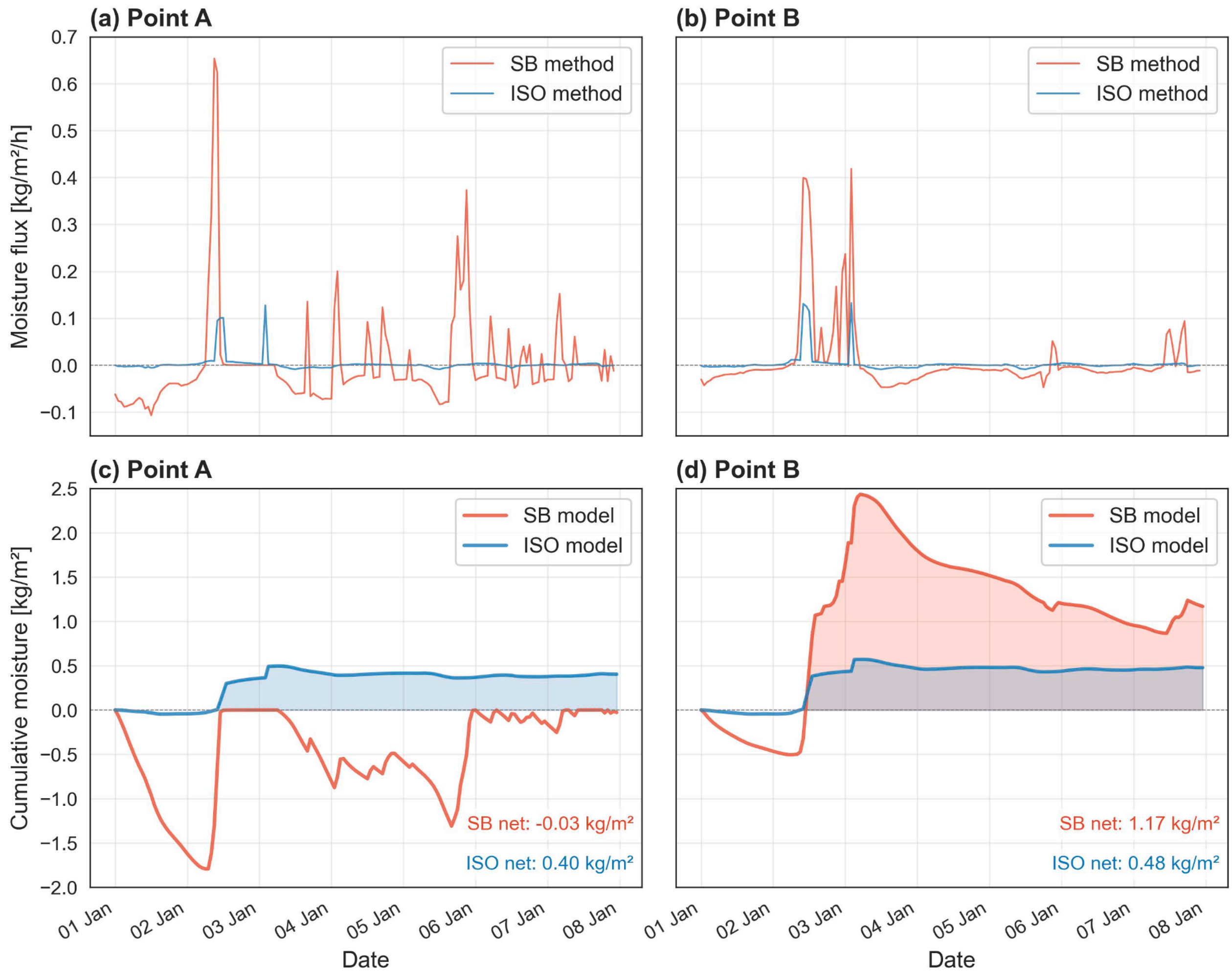

Fig. 8. Moisture flux (a, b) and cumulative moisture balance (c, d) in the outer brick layer (108 mm) at Point A (a, c) and Point B (b, d), comparing the SB and ISO driving rain calculation models for the simulation period 1-8 January 1995. Moisture flux is computed as the hourly change in total moisture content integrated over the full depth of the brick layer ($kg/m^2/h$), and cumulative balance is referenced to the start of the period. Positive values indicate net moisture uptake (wetting), negative values indicate drying.

content of 0.15 and a maximum of 0.49, accumulating 3.67 FTDR points during the period. Point B underwent 10 complete F-T cycles with an average saturation degree of ice content of 0.03 and a maximum of 0.11, accumulating 0.63 FTDR points. Compounded over the full 31-year simulation, these differences produce significant spatial variation in risk estimation, with the SB model's FTDR index ranging from 30 to 430 points across façade sections and averaging 240 (standard deviation = 140 points). The risk estimates for the ISO model are significantly lower, varying between 0 to 1.58 points across all façade sections. Fig. 14 compares the modeled FTDR-based risk spatially against the observed deterioration pattern.

As illustrated, neither risk mapping corresponds to the observed degradation pattern on the façade. Instead, they correspond to the outcomes of the critical F-T cycles analysis (Fig. 9 and Fig. 10) when assuming very high RH thresholds, i.e., 99% for the SB model and 95% for the ISO model. The SB model thus reflects its oval-shaped mapping of the RAF coefficient, as defined in Fig. 6, with the area of low risk at the center and high-risk areas near the edges. The ISO model, on the other hand, results in areas with either no or minimal FTDR index beneath the roof overhang and near the top left corner of the façade. From this location risk progressively increases towards the bottom right corner. Expectedly, comparing predicted FTDR index for individual façade sections with their corresponding level of degradation results in numerous over and underestimations, achieving weak correlations. SB model showed weak positive correlation with PCC = 0.14. Contrastingly, the ISO model shows weak negative relationship with PCC = -0.12.

5.2. *Results for solid brick ZO as an outer layer (sensitivity case)*

To test the sensitivity of the full façade hygrothermal assessment to the material properties, the critical F-T cycles analysis is repeated with the *Solid Brick ZO* type as the outer layer instead of the *Solid brick, extruded*. Among the fourteen RH threshold scenarios, the heatmaps derived from both SB and ISO models demonstrated the strongest correlation with observed degradation at the 85% threshold (0.31 and 0.61, respectively). The corresponding heatmaps are presented in Fig. 15. These heatmaps are directly compared with those derived using *Solid brick, extruded* as the outer layer. The latter were previously identified in Fig. 11 as the most representative of observed façade degradation and are using 90% and 75% RH thresholds for the SB and ISO models, respectively.

Despite having very different material properties, both brick types essentially resulted in very similar risk distributions across the façade, albeit with threshold-dependent shifts. ISO model-based results are nearly indistinguishable from each other as the scatter plot suggests with PCC value of 0.997. The SB heatmaps show minor differences, particularly in the middle area of the façade where the use of *Solid Brick ZO*

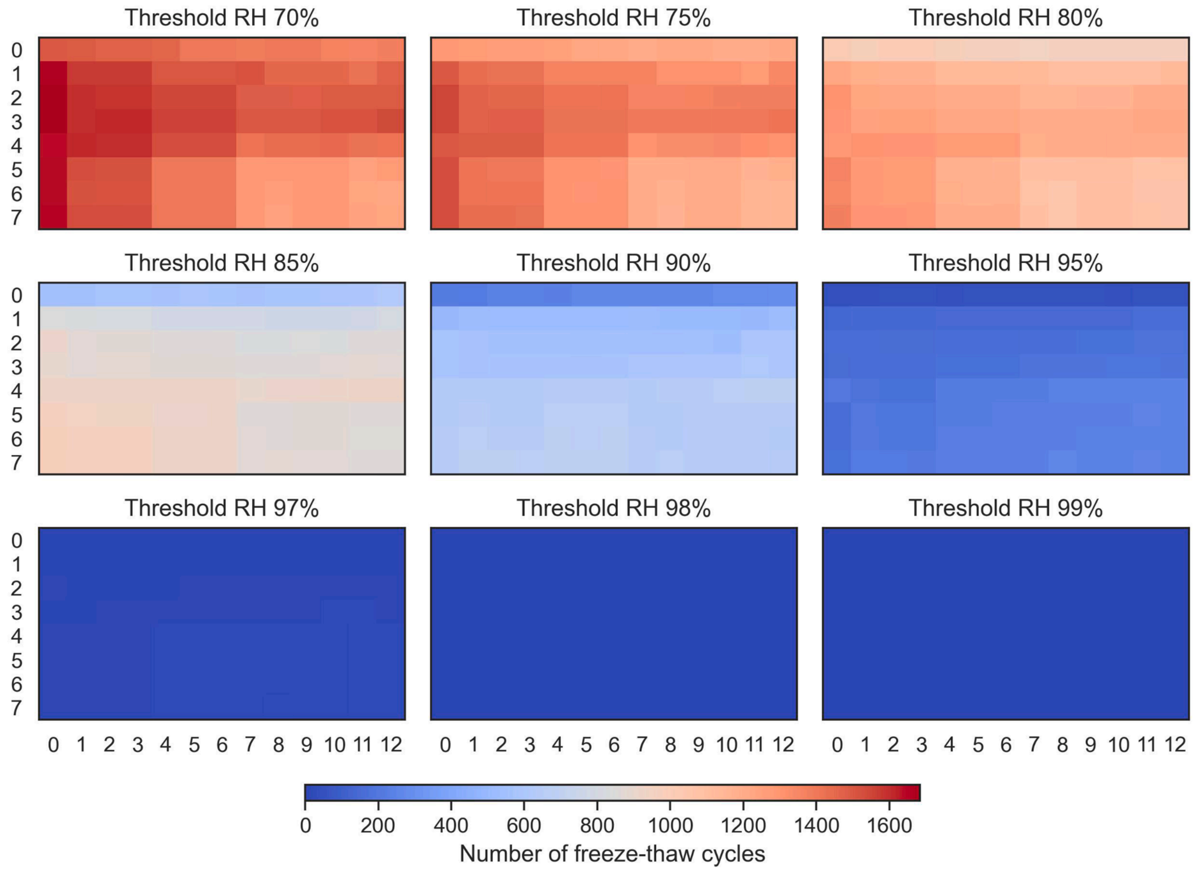

Fig. 9. Maps of F-T cycles frequency across the façade using different relative humidity thresholds and the ISO model.

resulted in higher number of F-T cycles. Structurally, however, the heatmaps follow the same pattern as the PCC value of 0.978, suggesting that it is the façade microclimate, rather than material properties, that dominates the spatial distribution of risk and degradation. The remaining heat maps, which are derived from using the *ZO brick* type as the outer layer and exhibit similar spatial patterns to those derived earlier, though with threshold-dependent shifts, are given in Appendix A.

6. Discussion

While the proposed methodology offers a practical approach to model hygrothermal degradation risks across entire façades, its case study accuracy showed to be reasonable yet limited when compared to the observed degradation.

6.1. Limitations of microclimate modeling

The inaccuracies in risk mappings stem primarily from microclimate modeling, as sensitivity testing of material properties showed. Altering the outer brick layer properties shifted the critical RH thresholds but left the spatial distribution of risk largely unchanged. This indicates that local microclimate, rather than material properties, drives the degradation pattern.

The main uncertainty lies in the semi-empirical WDR models. Solar irradiation and long-wave radiation were modeled using 3D tool accounting for surrounding buildings and roof overhang. The WDR models, however, incorporate only some microclimate aspects (e.g., wind-dependent wind speed), but oversimplify or omit others entirely, significantly affecting the risk mapping.

The SB model provides Rain Admittance Factor (RAF) mapping, allowing a fine distinction of incoming rain across the façade. Nevertheless, all three available RAF mappings assume open field conditions, ignoring obstructions and leaving WDR unscaled for suburban environment. This overemphasizes WDR relative to radiation variables, with RAF pattern dominating the final risk mappings. This is evident in the risk-mitigating effect of the roof overhang, which is not captured in the RAF mapping. Despite these limitations, the SB model's risk predictions remain credible with engineering-based interpretation: either manually adjusting the predicted risk in roof-adjacent sections (when using F-T cycles) or shifting the entire risk mapping downward to assign lower risk to these areas (when using the FTDR index).

Unlike the SB model, the ISO model does finely differentiate WDR across façades surfaces. Its Wall factor—the ISO counterpart to RAF mappings—is defined broadly for limited façade configurations. In this case study, a single value (0.4) applies to the entire façade. Additionally, the obstruction factor scales down WDR based on the distance to the nearest object (also 0.4). These reductions in WDR allow solar and long-wave radiation to exert greater influence on the risk mapping, resulting in predicted risk of degradation that more closely resembles the observed distribution.

An additional source of uncertainty concerns the climate dataset, which was generated under the A1B emissions scenario for the historical period 1991–2021. For this reason, the modeled dataset may deviate from locally measured conditions, providing further uncertainty in obtained risk mappings. Nevertheless, a continuous 31-year hourly sequence is preferable to repeatedly using a single design year, as it captures interannual climate variability, avoiding the bias introduced by selecting a representative year.

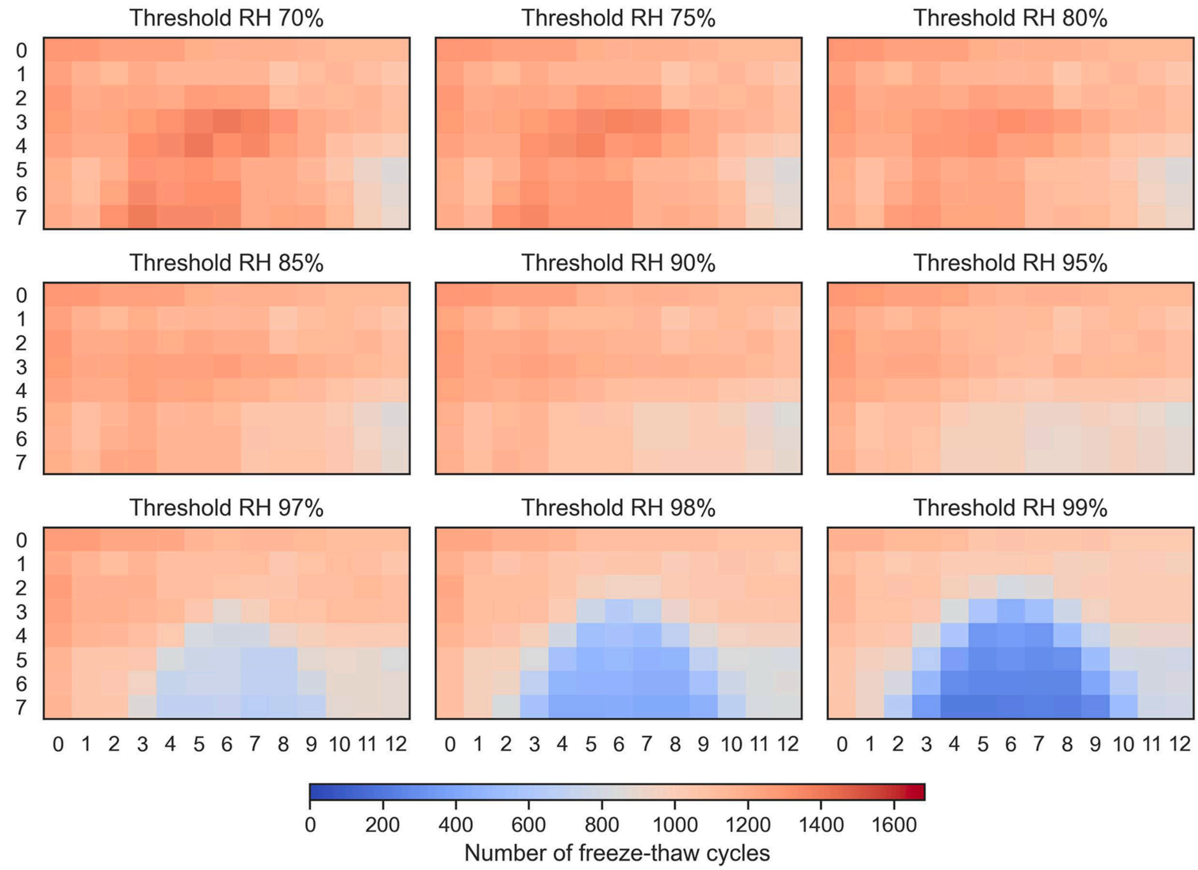

Fig. 10. Maps of freeze-thaw cycles frequency across the façade using different relative humidity thresholds and the SB model.

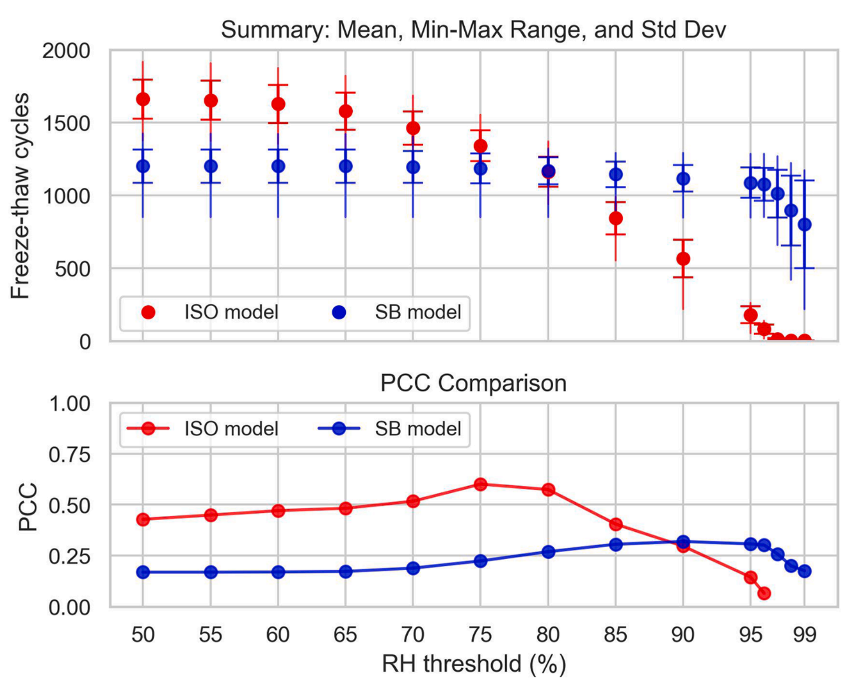

Fig. 11. Threshold analysis summary of freezing and thawing cycles aggregated from all façade sections. The error graph on top illustrates the average number of cycles for each threshold along with the corresponding standard deviation and minimum-maximum range. The bottom graph evaluates the similarity between the modelled risk mapping and the observed degradation distribution using the Pearson Correlation Coefficient (PCC)) for the ISO and SB models, respectively.

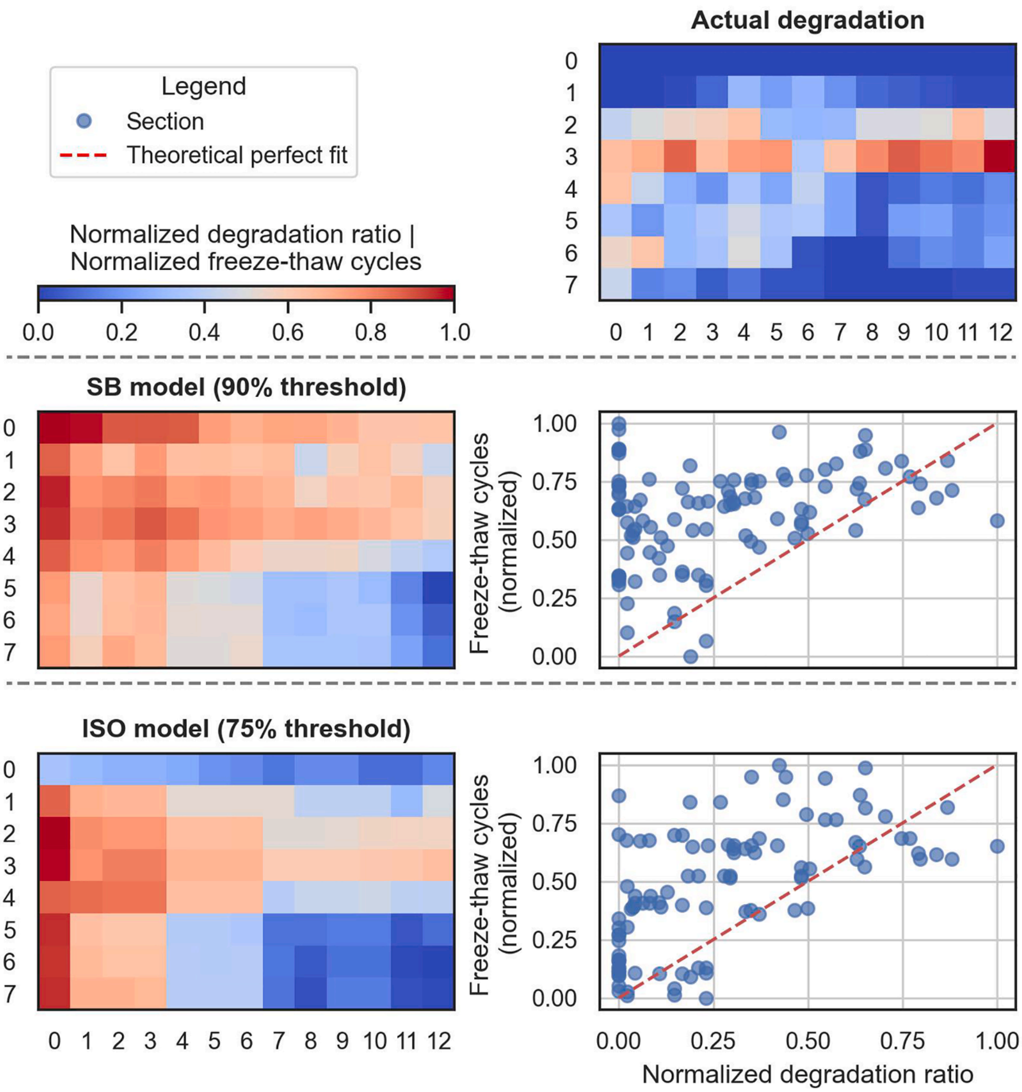

Fig. 12. Comparison of modeled F-T risk across the façade with observed deterioration patterns. The top-right heatmap shows the distribution of observed degradation. Heatmaps on the left show the mapping of the risk across the façade for the SB model (in the middle) and the ISO model (at the bottom). Scatterplots on the right compare the modeled risk with observed degradation across individual façade sections. For consistency, all values were normalized using min-max scaling (range: 0 and 1).

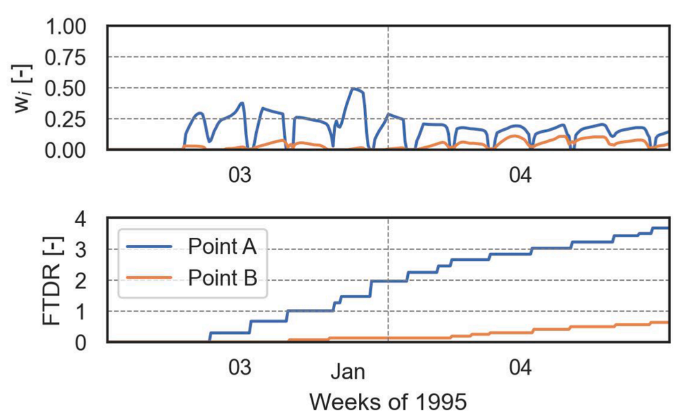

Fig. 13. Comparison of freezing-thawing behavior 5 mm behind the outer surface at points A and B during weeks 3-4 of representative 1995 using the SB model. Top: ice formation indicated by saturation degree of ice content (w_i). Bottom: cumulative sum of Freeze–thaw damage risk (FTDR) index.

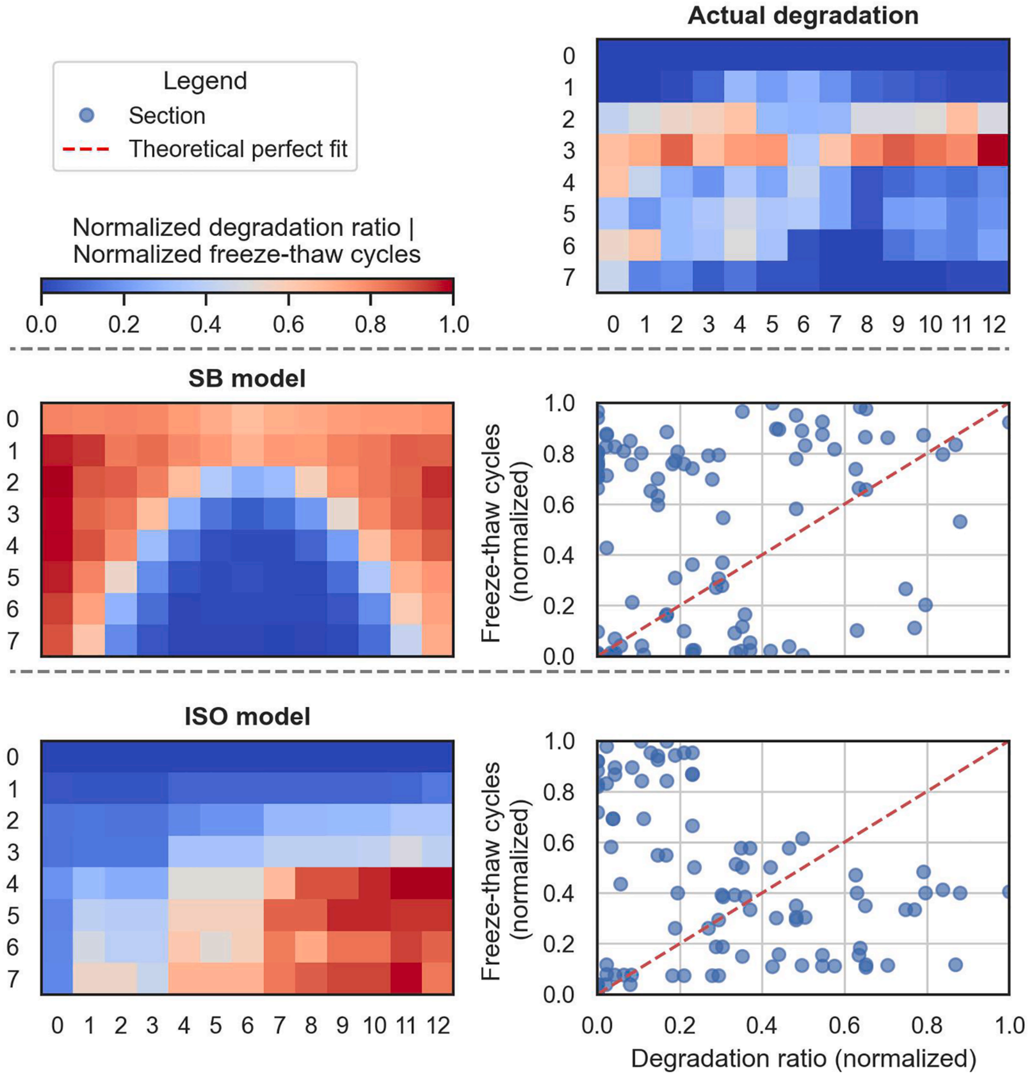

Fig. 14. Comparison of modeled FTDR-based risk across the façade with observed deterioration patterns. The top-right heatmap shows the distribution of observed degradation. Heatmaps on the left show the mapping of the FTDR index across the façade for the SB model (in the middle) and the ISO model (at the bottom). Scatterplots on the right compare the modeled risk with observed degradation across individual façade sections. For consistency, all values were normalized using min-max scaling (range: 0 and 1).

6.2. Limitations of performance indicators

Regardless of the WDR model used, risk estimates based on F-T cycles and the FTDR index have their own limitations, introducing further uncertainties into the resulting risk distributions over the façade.

Temperature conditions used to identify freezing and thawing represent the first limitation, assuming 0°C as a threshold when freezing occurs. In practice, water in porous materials may start freezing at lower temperatures due to freezing point depression. An alternate threshold such as -5°C could significantly decrease cycles counted in the analysis. This uncertainty, however, warrants further investigation.

Counting F-T cycles in bricks also relies on the critical degree of saturation (S_{crit}). Exceeding this threshold during a F-T event is linked to the physical distortion of bricks, allowing cycles to be counted in the analysis. Nevertheless, the S_{crit} of the outer brickwork is unknown as well as the other material characteristics. These were supplemented using WUFI's material database, which does not, however, contain any information on the S_{crit}.

To address this limitation, the case study used available degradation data to identify which RH thresholds produce risk mappings closest to the observed degradation pattern, assuming the optimal threshold corresponds to S_{crit}. At certain thresholds, predicted risk distributions began to resemble the observed degradation, suggesting the critical degree of saturation for the brick used. This finding was consistent across both materials tested (*Solid brick, extruded; Solid Brick ZO*). However, comparing SB and ISO models revealed a caveat: the most accurate risk mappings required different thresholds—90% for SB and 75% for ISO model (extruded bricks)

This discrepancy reflects methodological differences in moisture loads representation. The SB model produces higher WDR exposure, and consistently wetter outer layers, so F-T risk only emerges near saturation, hence the higher RH threshold. The ISO model produces a drier façade, requiring a lower RH threshold to reproduce the observed degradation pattern. Consequently, the RH threshold becomes a compensating parameter balancing differences in assumed moisture loads, rather than a direct measure of material properties. While both models can be calibrated to match observed degradation, the inferred S_{crit} is model-dependent and must be interpreted with caution.

Another insight comes from undamaged areas of the façade. These should correspond to low-risk areas in the modeling, yet both WDR models predicted over 800 F-T cycles above the RH threshold in all façade sections. This underscores that, in this context, F-T cycles should

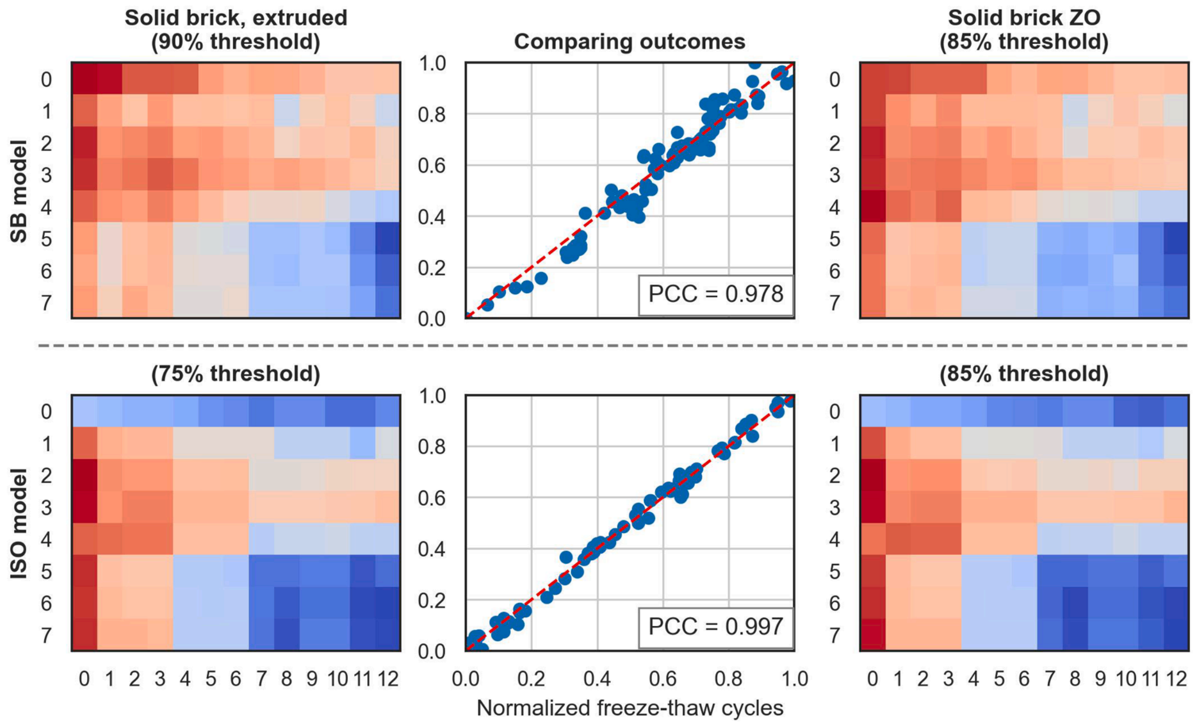

Fig. 15. Spatial comparison of freeze-thaw risk across the façade using the SB model (top row) and the ISO model (bottom row), with different outer brick types. Left: Solid brick, extruded. Right: Solid Brick ZO. Middle: Scatter plot comparing normalized freeze-thaw cycles between the two material configurations. Each dot represents one façade section.

be interpreted relatively: the methodology cannot yet link absolute cycle counts to the observed degradation, which would be necessary to infer degradation onset and progression.

Degradation risks were also analyzed using the FTDR index, which quantifies the risk based on ice content rather than cycle counts. However, the FTDR mappings corresponded to F-T cycle mappings at high RH thresholds (99% and 95% for SB and ISO, respectively), which is higher than the best-fit thresholds from cycle analysis (90% and 75%). This suggests the FTDR index underestimates risk across the façade. Consequently, while FTDR mappings correctly identify areas with little to no risk of degradation, they do not reflect the observed spatial degradation pattern. This may be due to uncertainties in WUFI's ice content approximation, as noted in Section 4.3.

7. Conclusion

This paper developed a methodology for assessing moisture-induced degradation risks across entire façades by combining existing engineering approaches for modelling the microclimate load on building façades with increased spatial resolution. The methodology was exemplified on a yellow brick façade with known degradation pattern, previously quantified across 104 façade sections using drone imagery and computer vision.

The accuracy of the F-T mappings varied across RH thresholds and WDR models. Increasing the threshold resulted in fewer cycles counted in the analysis, which impacted the distribution of risk across the façade. The ISO model with the 75% RH threshold achieved the best agreement with observed degradation (PCC = 0.6). A closer scrutiny of the discrepancies, primarily a misplacement of the highest-risk area on the façade, suggested limitations in the validation data. Specifically, the data considered only the number of spalled bricks in each façade section but not spalling severity. The most severely damaged bricks are located where the methodology predicted the highest risk, suggesting potentially higher accuracy than the PCC indicates. The SB model resulted in less accurate mappings (best PCC = 0.32 at 96% RH threshold), primarily due to not accounting for the roof overhang.

The discrepancy between optimal RH thresholds used in the WDR cases challenges assumption that the RH threshold equals the critical degree of moisture saturation S_{crit}. This was confirmed when repeating the analysis with different outer brick layer specifications (*Solid Brick ZO*), where similar risk maps were achieved using 85 % and 90% RH thresholds for the ISO and the SB models, respectively. Future work should focus on obtaining more precise material parameters.

Declaration of generative AI in scientific writing

During the preparation of this work the author(s) occasionally used Claude to polish and shorten the writing. After using these tools, the author(s) reviewed and edited the content as needed and take(s) full responsibility for the content of the published article.

Data availability

Data will be made available upon reasonable request.

CRediT authorship contribution statement

Jan Mandinec: Conceptualization, Methodology, Writing – review & editing, Writing – original draft, Investigation, Data curation, Visualization. **Angela Sasic Kalagasidis:** Conceptualization, Writing – review & editing, Supervision, Resources. **Pär Johansson:** Conceptualization, Writing – review & editing, Funding acquisition, Supervision, Resources.

Declaration of competing interest

The authors declare that they have no known competing financial interests or personal relationships that could have appeared to influence the work reported in this paper.

Acknowledgements

The authors are grateful for funding from the Swedish Research Council for sustainable development Formas (grant 2019-01402).

Supplementary materials

Supplementary material associated with this article can be found, in the online version, at doi:10.1016/j.buildenv.2026.114848.

References

[1] L. Thuvander, P. Femenías, K. Mjörnell, P. Meiling, Unveiling the process of sustainable renovation, Sustainability 4 (6) (2012) 1188–1213, https://doi.org/10.3390/su4061188.

[2] A. Farahani, H. Wallbaum, J.-O. Dalenbäck, Optimized maintenance and renovation scheduling in multifamily buildings – a systematic approach based on condition state and life cycle cost of building components, Constr. Manag. Econ. 37 (3) (2019) 139–155, https://doi.org/10.1080/01446193.2018.1512750.

[3] S. Jörk, Zustandsbewertung grosser Gebäudebestände, Schweiz Ing. Archit. (1998) 449–459.

[4] I.M. Shohet, M. Paciuk, Service life prediction of exterior cladding components under failure conditions, Constr. Manag. Econ. 24 (2) (2006) 131–148, https://doi.org/10.1080/01446190500184535.

[5] I.M. Shohet, M. Paciuk, Service life prediction of exterior cladding components under standard conditions, Constr. Manag. Econ. 22 (10) (2004) 1081–1090, https://doi.org/10.1080/0144619042000213274.

[6] M.F.S. Rodrigues, J.M.C. Teixeira, J.C.P. Cardoso, Buildings envelope anomalies: a visual survey methodology, Constr. Build. Mater. 25 (5) (2011) 2741–2750, https://doi.org/10.1016/J.CONBUILDMAT.2010.12.029.

[7] P.L. Gaspar, J. de Brito, Quantifying environmental effects on cement-rendered facades: a comparison between different degradation indicators, Build. Environ. 43 (11) (2008) 1818–1828, https://doi.org/10.1016/j.buildenv.2007.10.022.

[8] P. Gaspar and J. Brito, "Assessment of the overall degradation level of an element, based on field data," 2005. 10.13140/RG.2.1.2685.2563.

[9] M. N. Grussing, "Risk-based facility management approach for building components using a discrete Markov process – Predicting condition, reliability, and remaining service life," Ph.D., University of Illinois at Urbana-Champaign, United States – Illinois. Accessed 02 May 2022. [Online]. Available: https://www.proquest.com/docview/1815114326/abstract/63F8731FEA6240E9PQ/1.

[10] R. Edirisinghe, S. Setunge, G. Zhang, Markov model—based building deterioration prediction and ISO factor analysis for building management, J. Manag. Eng. 31 (6) (2015) 04015009, https://doi.org/10.1061/(ASCE)ME.1943-5479.0000359.

[11] S.M. Vieira, A. Silva, J.M.C. Sousa, J. de Brito, P.L. Gaspar, Modelling the service life of rendered facades using fuzzy systems, Autom. Constr. 51 (2015) 1–7, https://doi.org/10.1016/j.autcon.2014.12.011.

[12] A. Silva, J. de Brito, P.L. Gaspar, Application of the factor method to maintenance decision support for stone cladding, Autom. Constr. 22 (2012) 165–174, https://doi.org/10.1016/j.autcon.2011.06.014.

[13] M. Jerman, R. Černý, Effect of moisture content on heat and moisture transport and storage properties of thermal insulation materials, Energy Build. 53 (2012) 39–46, https://doi.org/10.1016/j.enbuild.2012.07.002.

[14] L.D. Hung Anh, Z. Pásztory, An overview of factors influencing thermal conductivity of building insulation materials, J. Build. Eng. 44 (2021) 102604, https://doi.org/10.1016/j.jobe.2021.102604.

[15] S. Rouchier, M. Woloszyn, G. Foray, J.-J. Roux, Influence of concrete fracture on the rain infiltration and thermal performance of building facades, Int. J. Heat. Mass Transf. 61 (2013) 340–352, https://doi.org/10.1016/j.ijheatmasstransfer.2013.02.013.

[16] Fuktcentrum, Industry standard ByggaF-method for moisture safety of construction process [Online]. Available, https://www.fuktcentrum.lth.se/verktyg_och_hjaelpmedel/fuktsaekert_byggande/byggaf_metoden/. (Accessed 16 January 2023).

[17] A. Hukka, H.A. Viitanen, A mathematical model of mould growth on wooden material, Wood. Sci. Technol. 33 (6) (1999) 475–485, https://doi.org/10.1007/s002260050131.

[18] E. Vereecken, L. Van Gelder, H. Janssen, S. Roels, Interior insulation for wall retrofitting – a probabilistic analysis of energy savings and hygrothermal risks, Energy Build. 89 (2015) 231–244, https://doi.org/10.1016/j.enbuild.2014.12.031.

[19] M. Uranjek, V. Bokan-Bosiljkov, Influence of freeze–thaw cycles on mechanical properties of historical brick masonry, Constr. Build. Mater. 84 (2015) 416–428, https://doi.org/10.1016/j.conbuildmat.2015.03.077.

[20] I. Netinger Grubeša, M. Vračević, J. Ranogajec, S. Vučetić, Influence of pore-size distribution on the resistance of clay brick to freeze–Thaw cycles, Materials 13 (10) (2020) 2364, https://doi.org/10.3390/ma13102364. Art. no.

[21] J. Yue, et al., Study on deterioration of gray brick with different moisture contents under freeze–Thaw environment, Materials 15 (5) (2022) 1819, https://doi.org/10.3390/ma15051819. Art. no.

[22] B. Funk, et al., Impact of freeze–thaw weathering on integrity, internal structure and particle release from micro- and nanostructured cement composites, Env. Sci.: Nano 6 (5) (2019) 1443–1456, https://doi.org/10.1039/C8EN01397G.

[23] Á. Török, B. Szemerey-Kiss, Freeze-thaw durability of repair mortars and porous limestone: compatibility issues, Prog. Earth. Planet. Sci. 6 (1) (2019) 42, https://doi.org/10.1186/s40645-019-0282-1. Art. no.

[24] N.W. Portal, A.W.M. van Schijndel, A.S. Kalagasidis, The multiphysics modeling of heat and moisture induced stress and strain of historic building materials and artefacts, Build. Simul. 7 (2014) 217–227, https://doi.org/10.1007/s12273-013-0153-4.

[25] P. Mensinga, J. Straube, C. Schumacher, Assessing the freeze-thaw resistance of clay brick for interior insulation retrofit projects, in: presented at the Thermal Performance of the Exterior Envelopes of Whole Buildings - 11th International Conference, Clearwater, Florida, USA, 2010 [Online]. Available: https://web.ornl.gov/sci/buildings/conf-archive/2010%20B11%20papers/203_Mensinga.pdf.

[26] P. Mensinga, Determining the Critical Degree of Saturation of Brick Using Frost Dilatometry, Ph.D. Thesis, University of Waterloo, Waterloo, Ontario, Canada, 2009.

[27] J. Kočí, J. Maděra, M. Keppert, R. Černý, Damage functions for the cold regions and their applications in hygrothermal simulations of different types of building structures, Cold. Reg. Sci. Technol. 135 (2017) 1–7, https://doi.org/10.1016/j.coldregions.2016.12.004.

[28] X. Zhou, D. Derome, J. Carmeliet, Hygrothermal modeling and evaluation of freeze-thaw damage risk of masonry walls retrofitted with internal insulation, Build. Environ. 125 (2017) 285–298, https://doi.org/10.1016/j.buildenv.2017.08.001.

[29] M. Thebault et al., A comparative study of simulation tools to model the solar irradiation on building façades. 2021. 10.18086/swc.2021.38.04.

[30] Ladybug Tools | about [Online]. Available: https://www.ladybug.tools/about.html. (Accessed 10 March 2025).

[31] Index, welcome to DL-Light, extension study daylit ambiance within SketchUp [Online]. Available: https://deluminaelab.com/dl-light/en/. (Accessed 10 March 2025).

[32] INDALUX software package for characterizing solar and daylight access in urban areas [Online]. Available: https://phybat.heia-fr.ch/idlx/. (Accessed 10 March 2025).

[33] J. Straube, E.F.P. Burnett, Simplified prediction of driving rain on buildings, international building physics conference. Eindhoven, Netherlands, 2000, pp. 375–382.

[34] S. Charisi, T.K. Thiis, P. Stefansson, I. Burud, Prediction model of microclimatic surface conditions on building façades, Build. Environ. 128 (2018) 46–54, https://doi.org/10.1016/j.buildenv.2017.11.017.

[35] S. Tsoka, T.K. Thiis, Calculation of the driving rain wall factor using ray tracing, J. Wind Eng. Ind. Aerodyn. 179 (2018) 190–199, https://doi.org/10.1016/j.jweia.2018.06.008.

[36] T.K. Thiis, I. Burud, A. Flø, D. Kraniotis, S. Charisi, P. Stefansson, Monitoring and simulation of diurnal surface conditions of a wooden façade, Procedia Environ. Sci. 38 (2017) 331–339, https://doi.org/10.1016/j.proenv.2017.03.088.

[37] S. Charisi, T.K. Thiis, P. Stefansson, I. Burud, Prediction model of microclimatic surface conditions on building façades, Build. Environ. 128 (2018) 46–54, https://doi.org/10.1016/j.buildenv.2017.11.017.

[38] B. Blocken, J. Carmeliet, Validation of CFD simulations of wind-driven rain on a low-rise building facade, Build. Environ. 42 (7) (2007) 2530–2548, https://doi.org/10.1016/j.buildenv.2006.07.032.

[39] A. Kubilay, D. Derome, B. Blocken, J. Carmeliet, Numerical simulations of wind-driven rain on an array of low-rise cubic buildings and validation by field measurements, Build. Environ. 81 (2014) 283–295, https://doi.org/10.1016/j.buildenv.2014.07.008.

[40] A. Khalilzadeh, H. Ge, H.D. Ng, Effect of turbulence modeling schemes on wind-driven rain deposition on a mid-rise building: CFD modeling and validation, J. Wind Eng. Ind. Aerodyn. 184 (2019) 362–377, https://doi.org/10.1016/j.jweia.2018.11.012.

[41] A. Kubilay, D. Derome, B. Blocken, J. Carmeliet, Wind-driven rain on two parallel wide buildings: field measurements and CFD simulations, J. Wind Eng. Ind. Aerodyn. 146 (2015) 11–28, https://doi.org/10.1016/j.jweia.2015.07.006.

[42] X. Zhou, A. Kubilay, D. Derome, J. Carmeliet, Comparison of wind-driven rain load on building facades in the urban environment and open field: a case study on two buildings in Zurich, Switzerland, Build. Environ. 233 (2023) 110038, https://doi.org/10.1016/j.buildenv.2023.110038. Art. no.

[43] A. Kubilay, D. Derome, J. Carmeliet, Coupling of physical phenomena in urban microclimate: a model integrating air flow, wind-driven rain, radiation and transport in building materials, Urban. Clim. 24 (2018) 398–418, https://doi.org/10.1016/j.uclim.2017.04.012.

[44] J. Toman, A. Vimmrová, R. Černý, Long-term on-site assessment of hygrothermal performance of interior thermal insulation system without water vapour barrier, Energy Build. 41 (1) (2009) 51–55, https://doi.org/10.1016/j.enbuild.2008.07.007.

[45] M. Morelli, E.B. MØller, Energy savings and risk of mold growth in apartments renovated with internal insulation, Sci. Technol. Built. Environ. 25 (9) (2019) 1199–1211, https://doi.org/10.1080/23744731.2019.1629241.

[46] M. Harrestrup, S. Svendsen, Full-scale test of an old heritage multi-storey building undergoing energy retrofitting with focus on internal insulation and moisture, Build. Environ. 85 (2015) 123–133, https://doi.org/10.1016/j.buildenv.2014.12.005.

[47] N.F. Jensen, T.R. Odgaard, S.P. Bjarløv, B. Andersen, C. Rode, E.B. Møller, Hygrothermal assessment of diffusion open insulation systems for interior retrofitting of solid masonry walls, Build. Environ. 182 (2020) 107011, https://doi.org/10.1016/j.buildenv.2020.107011. Art. no.

[48] N.F. Jensen, S.P. Bjarløv, C. Rode, B. Andersen, E.B. Møller, Hygrothermal performance of six insulation systems for internal retrofitting solid masonry walls, J. Build. Phys. 44 (6) (2021) 539–573, https://doi.org/10.1177/1744259120988745.

[49] T.K. Hansen, S.P. Bjarløv, R.H. Peuhkuri, M. Harrestrup, Long term in situ measurements of hygrothermal conditions at critical points in four cases of internally insulated historic solid masonry walls, Energy Build. 172 (2018) 235–248, https://doi.org/10.1016/j.enbuild.2018.05.001.

[50] P. Pagoni, E.B. Møller, R.H. Peuhkuri, N.F. Jensen, Evaluation of the performance of different internal insulation systems in real-life conditions - a case study, Build. Environ. 267 (2025) 112319, https://doi.org/10.1016/j.buildenv.2024.112319.

[51] N.F. Jensen, S.P. Bjarløv, C. Rode, E.B. Møller, Hygrothermal assessment of four insulation systems for interior retrofitting of solid masonry walls through calibrated numerical simulations, Build. Environ. 180 (2020) 107031, https://doi.org/10.1016/j.buildenv.2020.107031.

[52] P. Klõšeiko, E. Arumägi, T. Kalamees, Hygrothermal performance of internally insulated brick wall in cold climate: a case study in a historical school building, J. Build. Phys. 38 (5) (2015) 444–464, https://doi.org/10.1177/1744259114532609.

[53] X. Dang, E. Vereecken, H. Janssen, S. Roels, Hygrothermal response of masonry facades with vapour-tight or capillary-active internal insulation under current and future climate scenarios, Built. Herit. 9 (1) (2025) 23, https://doi.org/10.1186/s43238-025-00188-x. Art. no.

[54] J. McNally, C. Baldwin, C.A. Cruickshank, B. Conley, M. Carver, Monitoring and modelling of panelized overcladding retrofits in Canadian climate, J. Build. Phys. 0 (0) (2025) 489–495, https://doi.org/10.1007/978-981-97-8313-7_67.

[55] J. Hietikko, E. Tuominen, I. Valovirta, J. Vinha, The effects of increased thermal insulation in timber-framed external walls with a thin gypsum board as a wind barrier, J. Build. Phys. 49 (2) (2025) 237–260, https://doi.org/10.1177/17442591241309586.

[56] T. Odgaard, S.P. Bjarløv, C. Rode, Interior insulation – experimental investigation of hygrothermal conditions and damage evaluation of solid masonry façades in a listed building, Build. Environ. 129 (2018) 1–14, https://doi.org/10.1016/j.buildenv.2017.11.015.

[57] P. Johansson, P. Wahlgren, Deterioration in brick buildings: hygrothermal performance and measures to save them, in: E3S Web of Conferences, Tallinn, Estonia, 2020, https://doi.org/10.1051/e3sconf/202017223005.

[58] D.T. de Andrade, E. Bauer, J. Souza, Hygrothermal simulation applied to degradation modeling of ceramic facades, J. Perform. Constr. Facil 37 (1) (2023) 04022079, https://doi.org/10.1061/JPCFEV.CFENG-4247.

[59] N. Lindman, E. Lahdensivu, J. Lahdensivu, T. Pakkala, Delayed ettringite formation (DEF) and its effect on freeze-thaw damage in Finnish concrete façades, J. Build. Eng. 73 (2023) 106659, https://doi.org/10.1016/j.jobe.2023.106659. Art. no.

[60] T.A. Pakkala, J. Lahdensivu, P. Huuhka, Freeze-thaw damage dependence on wind-driven rain of outdoor exposed concrete – a case study, NCR 61 (2) (2019) 91–106, https://doi.org/10.2478/ncr-2019-0010.

[61] T. Pakkala, N. Lindman, J. Lahdensivu, Assessing climate change effects on freeze-thaw exposure of concrete structures, NCR 72 (1) (2025) 153–165, https://doi.org/10.2478/ncr-2025-0005.

[62] P.-Y. Wu, T. Johansson, S.O. Mundt-Petersen, K. Mjörnell, Probabilistic distributions of moisture damages in Swedish buildings, in: U. Berardi (Ed.), Multiphysics and Multiscale Building Physics, Springer Nature, Singapore, 2025, pp. 105–113, https://doi.org/10.1007/978-981-97-8305-2_13.

[63] S. Kyllingstad, T. Thiis, A. S. Flø, J. Potac, and M. Sýkora, "Climate, environment and frost damage of architectural heritage," in *Structures and Architecture - Proceedings of the 1st International Conference on Structures and Architecture, ICSA2010*, Accessed 9 July 2025. [Online]. Available: https://www.researchgate.net/publication/262709409_Climate_environment_and_frost_damage_of_architectural_heritage.

[64] X. Wang, J. Wang, Computer simulation of freeze-thaw cycle in Long'en Hall of Zhaoling Mausoleum in Shenyang City, China, in: 2022 International Conference on Computer Engineering and Artificial Intelligence (ICCEAI), 2022, pp. 148–152, https://doi.org/10.1109/ICCEAI55464.2022.00039.

[65] K. Ueno, J. Straube, R.V. Straaten, Field monitoring and simulation of a historic mass masonry building retrofitted with interior insulation, in: presented at the Thermal Performance of the Exterior Envelopes of Whole Buildings XII International Conference, Clearwater, Florida, USA, 2013, pp. 56–72.

[66] A. Arizzi, H. Viles, G. Cultrone, Experimental testing of the durability of lime-based mortars used for rendering historic buildings, Constr. Build. Mater. 28 (1) (2012) 807–818, https://doi.org/10.1016/j.conbuildmat.2011.10.059.

[67] B. Perrin, N.A. Vu, S. Multon, T. Voland, C. Ducroquetz, Mechanical behaviour of fired clay materials subjected to freeze–thaw cycles, Constr. Build. Mater. 25 (2) (2011) 1056–1064, https://doi.org/10.1016/j.conbuildmat.2010.06.072.

[68] C. Feng, S. Roels, H. Janssen, Towards a more representative assessment of frost damage to porous building materials, Build. Environ. 164 (2019), https://doi.org/10.1016/j.buildenv.2019.106343.

[69] G. Fagerlund, The critical degree of saturation method of assessing the freeze/thaw resistance of concrete, Mat. Constr. 10 (4) (1977) 217–229, https://doi.org/10.1007/BF02478693.

[70] J. Kočí, J. Maděra, M. Keppert, R. Černý, Damage functions for the cold regions and their applications in hygrothermal simulations of different types of building structures, Cold. Reg. Sci. Technol. 135 (2017) 1–7, https://doi.org/10.1016/j.coldregions.2016.12.004.

[71] J. Mandinec, A. Sasic Kalagasidis, P. Johansson, Predicting façade deterioration using machine learning approach with drone imagery and microclimate data, Autom. Constr. 178 (2025) 106443, https://doi.org/10.1016/j.autcon.2025.106443.

[72] V. Nik, Climate Simulation of an Attic Using Future Weather Data Sets - Statistical Methods for Data Processing and Analysis, Chalmers University of Technology, 2010 [Online]. Available: https://research.chalmers.se/en/publication/114053. (Accessed 11 March 2026).

[73] V. Naserentin, A. Logg, D. Wästberg, DTCC Builder: A mesh generator for automatic, efficient, and robust mesh generation for large-scale city modeling and simulation, J. Open. Source Softw. 8 (86) (2023), https://doi.org/10.21105/joss.04928.

[74] B. Blocken, J. Carmeliet, Overview of three state-of-the-art wind-driven rain assessment models and comparison based on model theory, Build. Environ. 45 (3) (2010) 691–703, https://doi.org/10.1016/j.buildenv.2009.08.007.

[75] N. Dingle, Y. Lee, Terminal fallspeeds of raindrops, J. Appl. Meteorol. Climatol. 11 (5) (1972) 877–879, https://doi.org/10.1175/1520-0450(1972)011<0877:TFOR>2.0.CO;2.

[76] A.C. Best, The size distribution of raindrops, Q. J. R. Meteorol. Soc. 76 (327) (1950) 16–36, https://doi.org/10.1002/qj.49707632704.

[77] J. Straube, Moisture control and enclosure wall systems, Ph.D. Thesis, University of Waterloo, Waterloo, Ontario, Canada, 1998.

[78] Fraunhofer Institute for Building Physics IBP, Wufi® 2d 4.4. https://wufi.de/en/software/wufi-2d/, Jun. 2022.

[79] A.S. Kalagasidis, T. Bednar, C.-E. Hagentoft, The evaluation of the interface moisture conductivity between control volumes. Comparison between linear, harmonic and integral averaging, in: 9th International Conference on Performance of the Exterior Envelopes of Whole Buildings. Clearwater Beach, Florida,2004, 2004 [Online]. Available: https://research.chalmers.se/en/publication/523363. (Accessed 15 January 2026).

[80] H.M. Künzel, Simultaneous heat and moisture transport in building components. One- and two-dimensional calculation using simple parameters, Ph.D. Thesis, Fraunhofer Institute of Building Physics, Suttgart, 1995.